理學碩士 學位論文

금속촉매를 이용한 ZnO 나노 막대의 성장과 응용에 관한 연구

Study on the growth and application of ZnO nanorods

2008年　2月

韓國海洋大學校　大學院

應用科學科

河 宣 如

理學碩士 學位論文

금속촉매를 이용한 ZnO 나노 막대의 성장과 응용에 관한 연구

Study on the growth and application of ZnO nanorods

指 導 敎 授

張 志 豪

2008年　2月

韓國海洋大學校　大學院

應用科學科

河 宣 如

本 論文을 河宣如의 理學碩士 學位論文으로 認准함.

위 원 장　　李 三 寧　　(인)

위　　원　　安 亨 秀　　(인)

위　　원　　張 志 豪　　(인)

2007 년　12 월　7 일

한국해양대학교 대학원

CONTENTS

국 문 요 약

본 논문에서는 다양한 금속촉매 위에 성장한 ZnO 나노막대의 광학적, 구조적 특성에 대한 평가와 이를 이용하여 제작한 ZnO 나노막대 소자의 전기적 특성에 대해 고찰하였다. 본 실험의 목적은 ZnO 나노막대의 성장조건의 최적화를 통해 다양한 금속촉매 위에서 성장한 ZnO 나노막대를 이용하여 나노 소자를 제작함에 있다. 제작한 나노소자의 광전류를 측정하므로서 자외선 검출기로서의 응용의 가능성을 제시하였다. 본 논문은 총 6장으로 구성되어 있으며 각장의 내용은 다음과 같다.

제 1장에서는 나노기술과 나노물질에 대한 소개와 나노구조 제작에 이용되는 다양한 성장방법 그리고 ZnO의 물질적 특성에 대하여 설명하였다. 제 2장에서는 제작된 ZnO 나노막대의 다양한 특성을 평가하기 위해 사용된 SEM, TEM, PL 그리고 HRXRD에 대해서 자세히 소개하였다. 제 3장에서는 새로운 금속촉매인 AuGe을 이용한 ZnO 나노막대의 촉매성장에 대해서 설명하였다. VPT 성장을 통한 ZnO 나노막대의 성장조건을 최적화 하였고, 이렇게 성장된 ZnO 나노막대의 광학적 특성과 나노막대의 기울어진 정도를 평가하였다. 제 4장에서는 성장온도와 캐리어 가스 흐름을 체계적으로 제어하여 나노막대의 성장에 미치는 영향에 대해서 알아보았다. 잘 정렬된 ZnO 나노막대는 ITO glass 위에서 성장하였으며, 단계적으로 성장온도를 제어함으로서 나노막대의 성장 매커니즘을 알 수 있

었다. 제 5장에서는 샌드위치 된 Si 기판을 이용하여 ZnO 나노막대 디바이스를 제작하였다. 먼저 다양한 금속 촉매를 이용하여 나노막대를 성장하였고 이를 통해 금속촉매의 종류에 따른 성장의 차이를 알 수 있었다. 제작된 나노막대 디바이스를 가지고 전기적 특성 평가와 광전류 특성 평가를 통해 자외선 검출기로써의 가능성을 확인할 수 있었다. 마지막으로 제 6장에서는 본 논문에서 얻어진 결과를 정리하여 결론을 기술하였다.

Abstract

In this thesis, the growth of ZnO nanorods and the application of ZnO nanorods such as UV detector has been studied. ZnO nanorods were grown by simple vapor-phase-transfortation (VPT) method and structural, optical and electrical characterization were performed. The feasibility of nanorods to an application for UV detector is investigated.

In the chapter 1, a brief introduction of nanomaterial and nanotechnology, growth process of ZnO nanostructures and the fundamental ZnO properties are described. The chapter 2 explains the principals of scanning electron microscopy (SEM), transmission electron microscopy (TEM), photoluminescence (PL) and high resolution x-ray diffraction (HRXRD). In the chapter 3, the growth conditions are investigated and the feasibility of AuGe as a novel catalyst is examined. ZnO nanostructures were grown by simple vapor phase transportation method in a function of growth temperature. In the chapter 4, the growth mechanism is studied through the ZnO nanorods grown on ITO glass. The growth rate of ZnO nanorods were controlled by growth parameters such as growth temperature and carrier gas flow. In the chapter 5, ZnO nanorod device by using sandwiched Si-substrates was investigated. Various metals were pre-deposited on the

Si-substrates and ZnO nanorods were grown on it. Electrical characterization and photocurrent properties were investigated by using a Shottky contact ZnO nanorods. In the chapter 6, the obtained results from this thesis are summarized and concluded.

Chapter 1. Introduction

1.1 Nanotechnology and nanomaterial

Nanotechnology deals with small structures or small-sized materials. The typical dimension spans from subnanometer to several hundred nanometers. A nanometer (nm) is one billionth of a meter, or 10^{-9} m. Fig. 1.1 gives a partial list of zero-dimensional nanostructures with their typical ranges of dimensions [1,2]. One nanometer is approximately the length equivalent to 10 hydrogen or 5 silicon atoms aligned in a line. Small features permit more functionality in a given space, but nanotechnology is not only a simple continuation of miniaturization from micron meter scale down to nanometer scale. Materials in the micrometer scale mostly exhibit physical properties the same as that of bulk form; however, materials in the nanometer scale may exhibit physical properties distinctively different from that of bulk. Materials in this size range exhibit some remarkable specific properties; a transition from atoms or molecules to bulk form takes place in this size range. For example, crystals in the nanometer scale have a low melting point (the difference can be as large as 1000 ^{o}C) and reduced lattice constants, since the number of surface atoms or ions becomes a significant fraction of the total number of atoms or ions and the

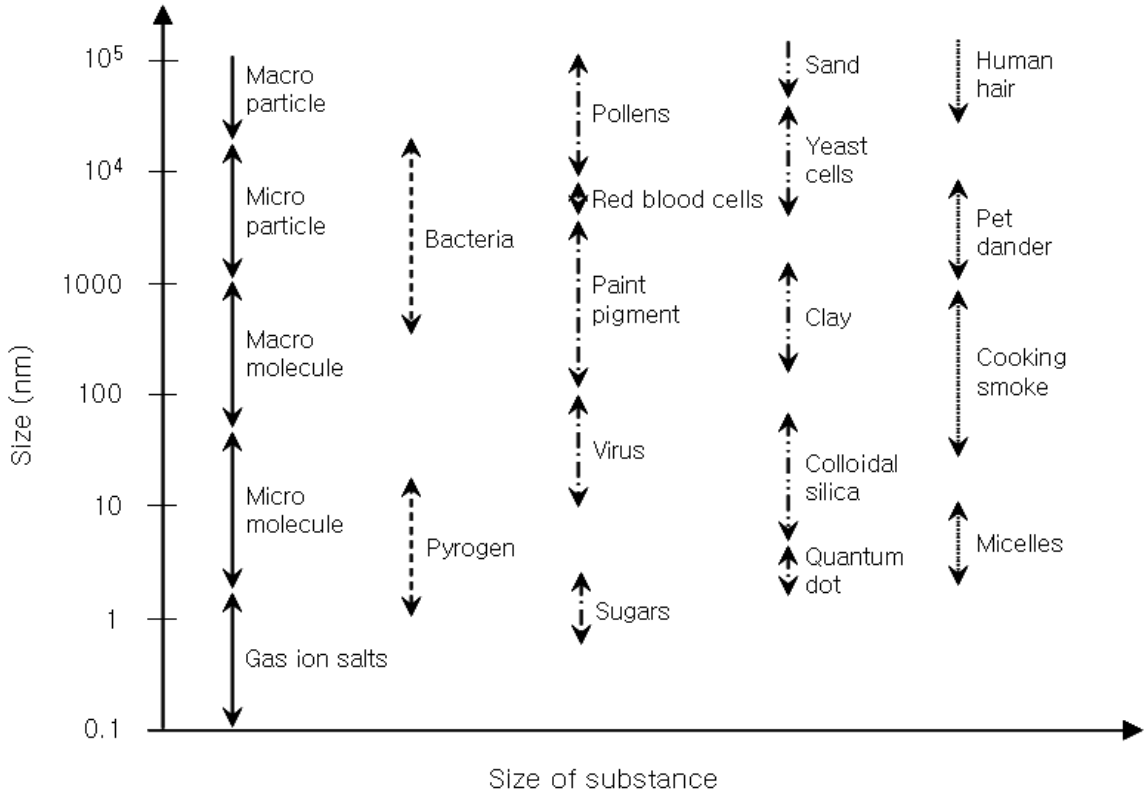

Fig. 1.1. Examples of zero-dimensional nanostructures or nanomaterials with their typical ranges of dimension.

surface energy plays a significant role in the thermal stability. Crystal structures stable at elevated temperatures are stable at much lower temperatures in nanometer sizes, so ferroelectrics and ferromagnetics may lose their ferroelectricity and ferromagnetism when the materials are shrunk to the nanometer scale. Bulk semiconductors become insulators when the characteristic dimension is sufficiently small (in a couple of nanometers). Although bulk gold does not exhibit catalytic properties, Au nanocrystal demonstrates to be an excellent low temperature catalyst.

Miniaturization is not necessarily limited to semiconductor-based electronics, though simple miniaturization already brings us significant excitement [3]. Promising application of nanotechnology in the practice of medicine, often referred to as nanomedicine, have attracted a lot of attention and have become a fast growing field.

1.2 Growth process of nanostructure

1.2.1 Spontaneous growth

Spontaneous growth is process driven by the reduction of Gibbs free energy of chemical potential. The reduction of Gibbs free energy is commonly realized by phase transformation or chemical reaction or the release of stress. For the formation of nanorods or nanowires, anisotropic growth is required, i.e. the crystal grows along a certain orientation faster than other directions. Uniformly sized nanowires, i.e. the same diameter along the longitudinal direction of a given nanowire, can be obtained when crystal growth proceeds along one direction, whereas no growth along other directions. In spontaneous growth, for given material and growth conditions, defects and impurities on the growth surface can play a significant role in determining the morphology of the final products.

1.2.2 Template-based synthesis

Template-based synthesis of nanostructured materials is a very general method and can be used in fabrication of nanorods, nanowires and nanotubules of polymer, metals, semiconductors and oxides. Various templates with nanosized channels have been explored for the template growth of nanorods and nanotubules. The most commonly used and commercially available templates are anodized alumina membrane [4], radiation track-etched polymer membranes [5]. Other membranes have also been used as templates such as nanochannel array glass [6], radiation track-etched mica [7], and mesoporous material [8], porous silicon by electrochemical etching of silicon wafer [9], zeolites [10] and carbon nanotubes [11,12]. Alumina membranes with uniform and parallel porous structure are made by anodic oxidation of aluminum sheet in solutions of sulfuric, oxalic, or phosphoric acids [4,13]. The pores are arranged in a regular hexagonal array, and densities as high as 10^{11} pores/cm^2 can be achieved [14]. Pore size ranging from 10 nm to 100 μm can be created [14,15]. The polycarbonate membranes are made by bombarding a nonporous polycarbonate sheet, with typical thickness ranging from 6-20 μm, with nuclear fission fragments to create damage tracks, and then chemically etching these tracks into pores [5]. In radiation track etched membranes, pores have a uniform size as small as 10 nm, though randomly distributed. Pore densities can be as high as 10^9 pores/cm^2.

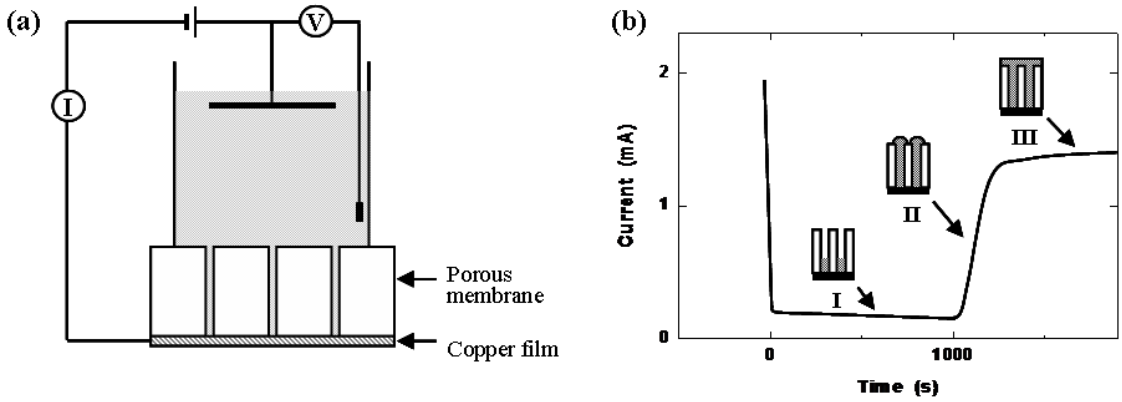

Fig. 1.2. Common experimental set-up for the template-based growth of nanowires using electrochemical deposition. (a) Schematic illustration of electrode arrangement for deposition of nanowires. (b) Current-time curve for electrodeposition of Ni into a polycarbonate membrane with 60 nm diameter pores at -1.0 V. Insets depict the different stages of the electrodeposition.

Fig. 1.2 illustrates the common set-up for the template-based growth of nanowires using electrochemical deposition.

Kinetically, enough surface relaxation permits maximal packing density, so a diffusion-limited process is preferred. Other considerations include the easiness of release of nanowires or nanorods from the templates and of handling during the experiments.

1.2.3 Electrospinning

Electrospinning, also know as electrostatic fiber processing, technique has been originally developed for generating ultrathin polymer fibers [16,17]. Electrospinning uses electrical forces to produce

polymer fibers with nanometer-scale diameters. Electrospinning occurs when the electrical forces at the surface of a polymer solution or melt overcome the surface tension and cause an electrically charged jet to be ejected. When the jet dries or solidifies, an electrically changed fiber remains. This charged fiber can be directed or accelerated by electrical forces and then collected in sheets or other useful geometrical forms. More than 30 polymer fibers with diameters ranging from 40 nm to 500 nm have been successfully produced by electrospinning [18,19]. The morphology of the fibers depends on the process parameters, including solution concentration, applied electric field strength, and the feeding rate of the precursor solution. Recently, electrospinning has also been explored for the synthesis of ultrathin organic-inorganic hybrid fibers [20-23].

1.2.4 Lithography

Lithography represents another route to the synthesis of nanowires. Various techniques have been explored in the fabrication of nanowires, such as electron bean lithography, [24,25] ion beam lithography, STM lithography, X-ray lithography, proxial-probe lithography and near-field photolithography [26]. Nanowires with diameter less than 10 nm and an aspect ratio of 100 can be readily

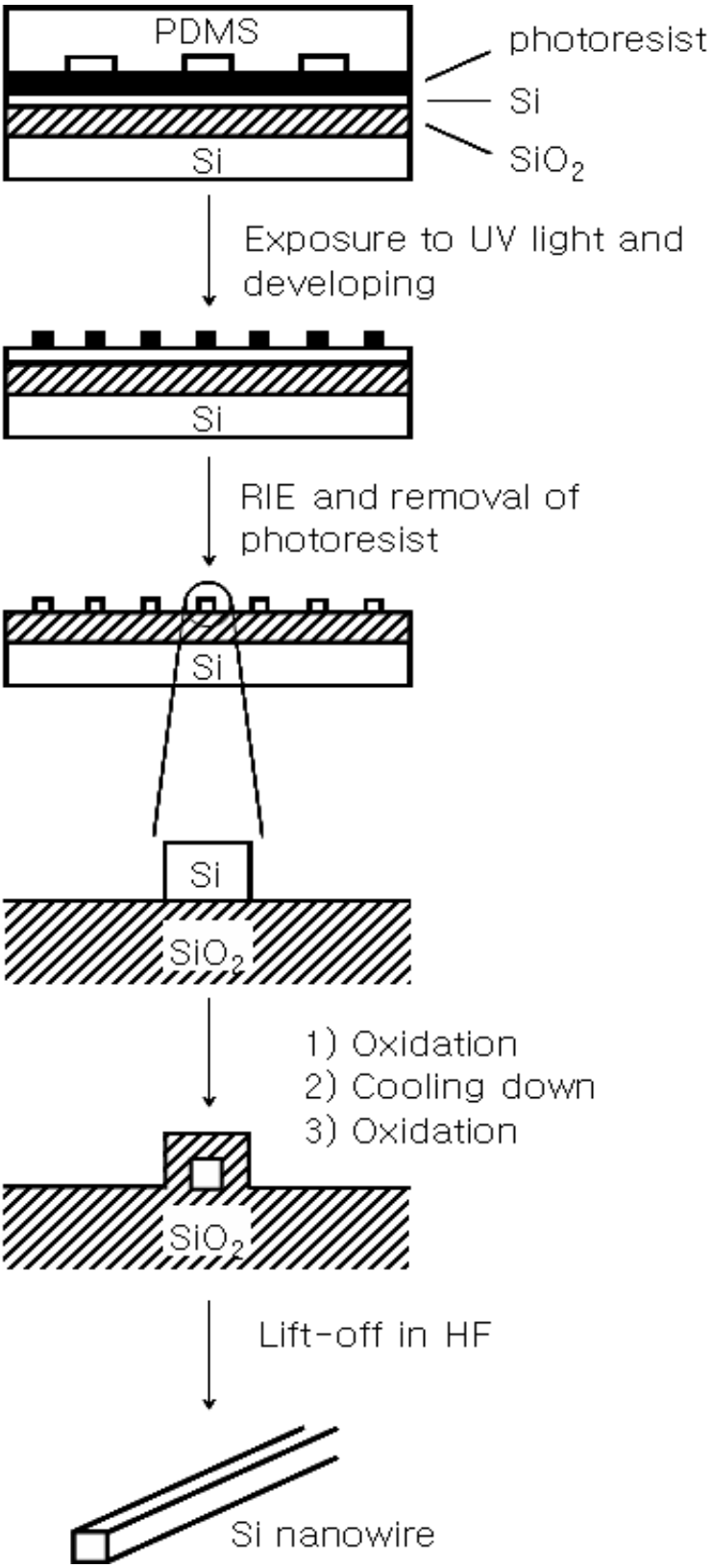

Fig. 1.3. Schematic illustrating procedeures used for the preparation of single crystal silicon nanowires.

prepared. Fig. 1.3 outlines the schematic procedures used for the preparation of single crystal silicon nanowire [27]. The nanoscale features were defined in a thin film of photoresist by exposing it to a UV light source through a phase shift mask made of a transparent elastomer, such as poly (PDMS). The light passing through this phase mask was modulated in the near-filed such that an array of nulls in the intensity were formed at the edges of the relief structures patterned on the PDMS mask. Therefore, nanoscale features were generated in a thin film of photoresist and the patterns were transferred into the underlying substrate using a reactive ion etching or wet etching process. Silicon nanostructures were separated from underlying substrate by slight over-etching.

1.3 Material properties of ZnO

The semiconductor ZnO is fueled and fanned by its prospects in optoelectronics applications owing to its direct wide band gap (3.437 eV at 2 K and 3.37 eV at RT). The interest in ZnO has large exciton binding energy of 60 meV which is much larger than those of GaN (24 meV), ZnSe (19 meV), and GaAs (4.2 meV) as listed in table 1.1. ZnO also has much simpler crystal-growth technology, resulting in a potentially lower cost for ZnO-based devices. Table 1.1 provides a comparison of important properties that demonstrate some promising

features of the ZnO system.

The large exciton binding energy of ~60 meV paves the way for an intense near-band-edge excitonic emission at room and higher temperatures, because this value is 2.4 times that of the room-temperature (RT) thermal energy (k_BT=25 meV). It should be noted that besides the above-mentioned properties of ZnO, there are additional properties which make it preferable over other wide-band-gap materials: its high-energy radiation stability and amenability to wet chemical etching [28]. ZnO is easily etched in all acids and alkalis, and this provides an opportunity for fabrication of small-size devices.

Table 1.1. Comparison of structural and optical properties of ZnO with other materials.

Materials	Crystal structure	Lattice constants		Bandgap energy (eV)	Cohesive energy (eV)	Exciton binding energy (meV)
		a (Å)	c (Å)			
ZnO	Wurtzite	3.249	5.207	3.37	1.89	60
ZnS	Wurtzite	3.823	6.261	3.8	1.59	39
ZnSe	Zinc blende	5.668	—	2.7	1.29	19
GaN	Wurtzite	3.189	5.185	3.39	2.24	24
GaAs	Zinc blende	5.653	—	1.42	1.63	4.9

ZnO has recently found other niche applications as well, such as fabrication of transparent transistors, where the protective covering

preventing light exposure is eliminated since ZnO-based transistors are insensitive to visible light. Also up to 2×10^{21} cm^{-3} charge carriers can be introduced by heavy substitutional doping into ZnO. By controlling the doping level electrical properties can be changed from insulator through *n*-type semiconductor to metal while maintaining optical transparency that makes it useful for transparent electrodes in flat-panel displays and solar cells.

1.4 Objective and organization of this research

One-dimensional (1D) nanostructure materials, such as nanorods, nanowires and nanotubes, have attracted much attention because of their interesting properties for understanding fundamental physical concepts and for potential applications. In particular, the electronic and optical properties of nanostructured materials have been of interest because of their potential application in the fabrication of microelectronic and optoelectronic devices.

The objective of this research is to grow well-aligned ZnO nanorods by vapor-phase-transfortation (VPT) method for the application to UV detector. In order to achieve this purpose, we have systematically made progress. First of all, optimum growth conditions are obtained through controlled growth parameters and then the growth mechanism of ZnO nanorods grown on ITO glass are investigated.

Finally, feasibility of application as an UV detector is demonstrated.

The chapter 2 describes the growth method of nanorods using metal catalyst. Experimental setups and theoretical backgrounds for scanning electron microscopy (SEM), transmission electron microscopy (TEM), photoluminescence (PL) and high resolution x-ray diffraction (HRXRD) measurements are depicted. In the chapter 3, the growth conditions are investigated and the feasibility of AuGe as a novel catalyst is examined in terms of the uniformity and high optical quality of nanorods. ZnO nanostructures were grown by simple vapor phase transportation method in a function of growth temperature. As a new catalyst, which confirms both controllable growth and high crystallinity of ZnO nanorods, AuGe is introduced. In the chapter 4, the growth mechanism is studied through the ZnO nanorods grown on ITO glass. The growth rate of ZnO nanorods were controlled by growth parameters such as growth temperature and carrier gas flow. Optical chracterization of ZnO nanorods was discussed. In the chapter 5, ZnO nanorod device using sandwiched Si-substrates has been investigated. Various metals were pre-deposited on the Si-substrates and ZnO narods were grown on it. Electrical characterization and photocurrent were performed on Shottky diode using ZnO nanorods. In the chapter 6, we summarize and conclude this research. Photoluminescence properties of high quality ZnO tetrapods and study on the electronic state in ZnO:In

nanostructures by In contents are given in appendix.

REFERENCES

[1] *Microscopy and Histology Catalog*, Polyscience, Warrington, PA, 1993-1994.

[2] N. Itoh, in *Functional Thin Films and Functional Materials: New Concepts and Technology*, Tsinghua University Press and Springer-Verlag, p.1 2003

[3] R.P. Feynman, *J. Microelectromechan. Syst.* 1 (1992) 1

[4] R.C. Furneaux, W.R. Rigby, and A.P. Davidson, *Nature* 337 (1989) 147

[5] R.L. Fleisher, P.B. Price, and R.M. Walker, *Nuclear Tracks in Solid*, University of California Press, Berkeley, CA, 1975

[6] R.J. Tonucci, B.L. Justus, A.J. Campillo and C.E. Ford, *Science* 258 (1992) 783

[7] G.E. Possin, *Rev. Sci. Instrum.* 41 (1970) 772

[8] C. Wu and T. Bein, *Science* 264 (1994) 1757

[9] S. Fan, M.G. Chaplin, N.R. Franklin, T.W. Tombler, A.M. Cassell, and H. Dai, *Science* 283 (1999) 512

[10] P. Enzel, J.J. Zoller, and T. Bein, *Chem. Commun.* 633 (1992)

[11] C. Guerret-Piecourt, Y. Le Bouar, A. Loiseau, and H. Pascard, *Nature* 372 (1994) 761

[12] P.M. Ajayan, O. Stephan, and C. Colliex, *Nature* 375 (1995) 564

[13] A. Despic and V.P. Parkhuitik, *Modern Aspects of Electrochemistry*, Vol. 20 Plenum, 1989

[14] D.AlMawiawi, N. Coombs, and M. Moskovits, *J. Appl. Phys.* 70 (1991) 4421

[15] C.A. Foss, M.J. Tierney, and C.R. Martin, *J. Phys. Chem.* 96 (1992) 9001

[16] A. Frenot and I.S. Chronakis, *Current Opin. Colloid Interf. Sci.* 8 (2003) 64

[17] D.H. Reneker and I. Chun, *Nanotechnolgy* 7 (1996) 216

[18] H. Fong, W. Liu, C.S. Wang, and R.A. Vaia, *Polymer* 43 (2002) 775

[19] J.A. Mathews, G.E. Wnek, D.G. Simpson, and G.L. Bowlin, *Biomacromolecules* 3 (2002) 232

[20] G. Larsen, R. Velarde-Ortiz, K. Minchow, A. Barrero, and I.G. Loscertales, *J. Am. Chem. Soc.* 125 (2003) 1154

[21] H. Dai, J. Gong, H. Kim, and D. Lee, *Nanotechnology* 13 (2002) 674

[22] D. Li and Y. Xia, *Nano Lett.* 3 (2003) 555

[23] D. Li and Y. Xia, in *Nnanomaterials and Their Optical Applications*, SPIE Proceedings 5224 (2003)

[24] K. Kurihara, K. Iwadate, H. Namatsu, M. Nagase, and K. Murase, *J. Vac. Sci. Technol.* B13 (1995) 2170

[25] H.I. Liu, D.K. Biegelsen, F.A. Ponce, N.M. Johnson, and R.F. Pease, *Appl. Phys. Lett.* 64 (1994) 1383

[26] Y. Xia, J.A. Rogers, K.E. Paul, and G.M. Whitesides, *Chem. Rev.* 99 (1999) 1823

[27] Y. Yin, B. Gates, and Y. Xia, *Adv. Mater.* 12 (2000) 1426

[28] D.C. Look, *Mater. Sci. Eng.* B80 (2001) 381

Chapter 2. Experimental

2.1 Growth of nanostructure

2.1.1 Non-catalytic growth

The driving force for the synthesis of nanorods and nanowires by non-catalyst growth is a decrease in Gibbs free energy, which arises from either recrystallization or a decrease in supersaturation. Nanowires and nanorods grown by evaporation-condensation methods are commonly single crystals with fewer imperfections. Crystal growth can be generally considered as a heterogeneous reaction, and a typical crystal growth proceeds following the sequences, as sketched in Fig. 2.1.

(1) Diffusion of growth species from the bulk (such as vapor or liquid phase) to the growing surface, which, in general, is considered to proceed rapid enough and, thus, not at a rate limiting process.

(2) Adsorption and desorption of growth species onto and from the growing surface. This process can be rate limiting, if the supersaturation or concentration of growth species is low.

(3) Surface diffusion of adsorbed growth species. During surface diffusion, an adsorbed species may either be incorporated into a growth site, which contributes to crystal growth, or escape from

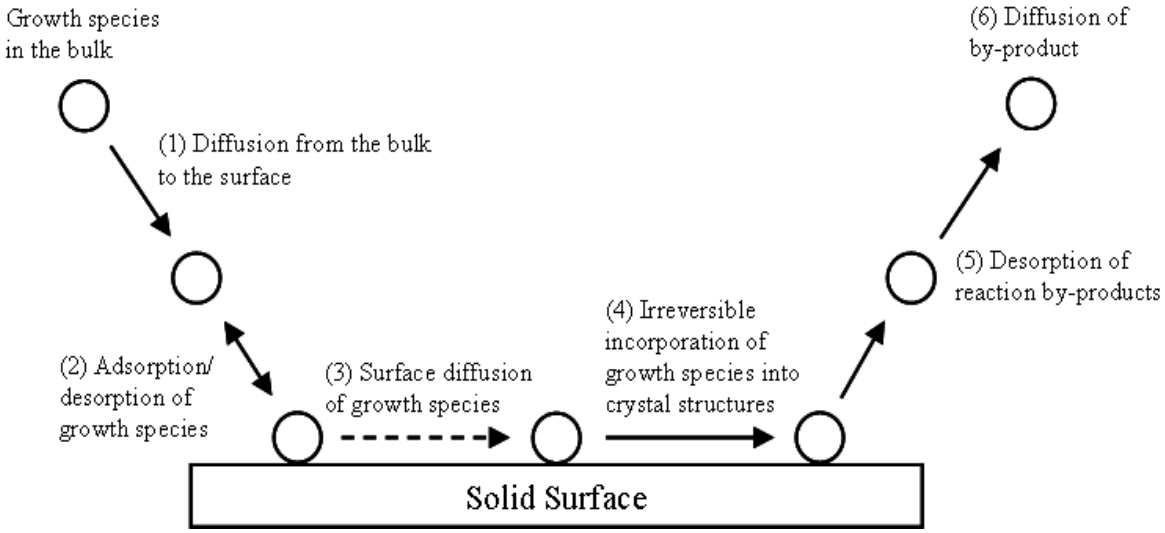

Fig. 2.1. Schematic illustrating six steps in crystal growth, which can be generally considered as a heterogeneous reaction, and a typical crystal growth proceeds following the sequences.

the surface.

(4) Surface growth by irreversibly incorporating the adsorbed growth species into the crystal structure. When a sufficient supersaturation or a high concentration of growth species is present, this step will be the rate-limiting process and determines the growth rate.

(5) If by-product chemicals were generated on the surface during the growth, by-products would desorb from the growth surface, so that growth species can adsorb onto the surface and the process can continue.

(6) By-product chemicals diffuse away from the surface so as to vacate the growth sites for continuing growth.

For most crystal growth, rate-limiting step is either adsorption-desorption of growth species on the growth surface (step 2) or surface growth (step 4). When step 2 is rate limiting, the growth rate is determined by condensation rate, J (atoms/cm^{2}sec), which is dependent on the number of growth species adsorbed onto the growth surface, which is directly proportional to the vapor pressure or concentration, P, of the growth species in the vapor as given by:

$$J = \frac{\alpha \sigma P_0}{\sqrt{2\pi m k T}} \tag{2.1}$$

where α is the accommodation coefficient, $\sigma = (P - P_0)/P_0$ is the supersaturation of the growth species in the vapor in which P_0 is the equilibrium vapor pressure of the crystal at temperature T, m is the atomic weight of the growth species and k is Boltzmann constant. α is the fraction of impinging growth species that becomes accommodated on the growing surface, and is a surface specific property. A surface with a high accommodation coefficient will have a high growth rate as compared with low α surfaces.

2.1.2 Catalytic growth

In the catalytic growth, a second phase material, commonly referred to as either impurity or catalyst, is purposely introduced to direct and confine the crystal growth on to a specific orientation and within a confined area. A catalyst forms a liquid droplet by itself or

by alloying with growth material during the growth, which acts as a trap of growth species. Enriched growth species in the catalyst droplets subsequently precipitates at the growing surface resulting in the one-directional growth.

(1) The catalyst or impurity must form a liquid solution with the crystalline material to be grown at the deposition temperature,

(2) The distribution coefficient of the catalyst or impurity must be less than unity at the deposition temperature.

(3) The equilibrium vapor pressure of the catalyst or impurity over the liquid droplet must be very small. Although the evaporation of the catalyst does not change the composition of the saturated liquid composition, in does reduce the total volume of the liquid droplet. Unless more catalyst is supplied, the volume of the liquid droplet reduce. Consequently, the diameter of the nanowire will reduce and the growth will eventually stop, when all the catalyst is evaporated.

(4) The catalyst or impurity must be inert chemically. It must not react with the chemical species such as by-products presented in the growth chamber.

(5) The interfacial energy plays a very important role. The wetting characteristics influence the diameter of the grown nanowire. For a given volume of liquid droplet, a small wetting angle results in a

large growth area, leading to a large diameter of nanowires.

(6) For a compound nanowire frowth, one of the constituents can serve as the catalyst.

(7) For controlled unidirectional growth, the solid-liquid interface must be well defined crystallographically. One of the simplest methods is to choose a single crystal substrate with desired crystal orientation.

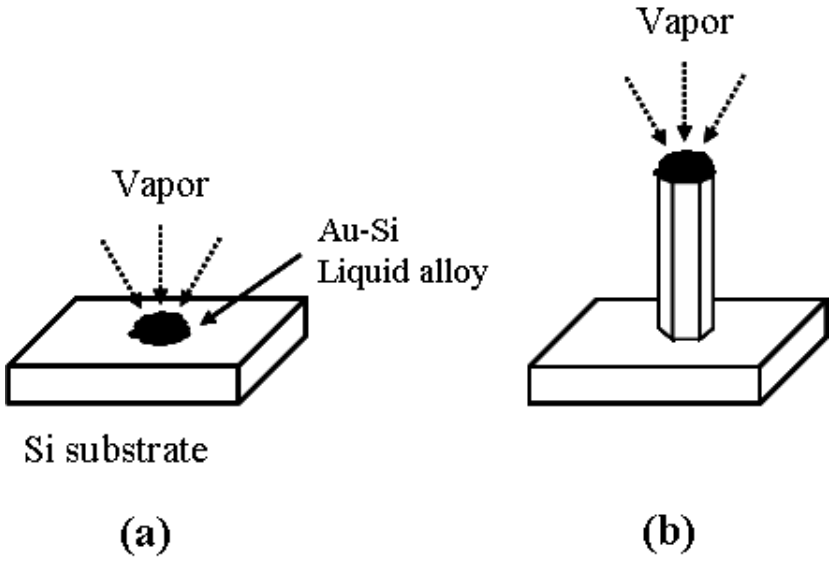

Fig. 2.2 Schematic showing the principal steps of the vapor-liquid-solid growth technique: (a) initial nucleation and (b) continued growth.

In a VLS growth, the process can be simply described as following as sketched in Fig. 2.2. The growth species is evaporated first, and then diffuses and dissolves into a liquid droplet. The surface of the liquid has a large accommodation coefficient, and is therefore a

preferred site for deposition. Saturated growth species in the liquid droplet will diffuse to and precipitate at the interface between the substrate and the liquid. The precipitation will first follow nucleation and then crystal growth. Continued precipitation or growth will separate the substrate and the liquid droplet, resulting in the growth of nanowires [1-2].

2.2 Characterization

2.2.1 Scanning electron microscopy (SEM)

SEM is one of the most widely used techniques used in characterization of nanomaterials and nanostructures. The resolution of the SEM approaches a few nanomaterials, and the instruments can operate at magnifications that are easily adjusted from ~10 to over 300,000.

In a typical SEM, a source of electrons is focused into a beam, with a very fine spot size of ~5 nm and having energy ranging from a few hundred eV to 50 KeV, that is rastered over the surface of the specimen by deflection coils. As the electrons strike and penetrate the surface, a number of interactions occur that result in the emission of electrons and photons from the sample, and SEM images are produced by collecting the emitted electrons on a cathode ray tube (CRT). Various SEM techniques are differentiated on the basis of what is

subsequently detected and imaged, and the principle images produced in the SEM are of three types: secondary electron images, backscattered electron images and elemental X-ray maps. When a high-energy primary electron interacts with an atom, it undergoes either inelastic scattering with atomic electrons or elastic scattering with the atomic nucleus. In an inelastic collision with an electron, the primary electron transfers part of its energy to the other electron. When the energy transferred is large enough, the other electron will emit from the sample. If the emitted electron has energy of less than 50 eV, it is referred to as a secondary electron. Backscattered electrons are the high-energy electrons thar are elastically scattered and essentially possess the same energy as the incident or primary electrons. The probability of backscattering increases with the atomic number of the sample material. Although backscattering images cannot be used for elemental identification, useful contrast can develop between regions of the specimen that differ widely in atomic number, Z. An additional interaction in the SEM is that the primary electron collides with and ejects a core electron from an atom in the sample. The excited atom will decay to its ground state by emitting either a characteristic X-ray photo or an Auger electron, both of which have been used for chemical characterization and will be discussed later in this chapter. Combining with chemical analytical capabilities, SEM not only provides

the image of the morphology and microstructures of bulk and nanostructured materials and devices, but can also provide detailed information of chemical composition and distribution.

The theoretical limit to an instrument's resolving power is determined by the wavelengths of the electron beam used and the numerical aperture of the system. The resolving power, R, of an instrument is defined as:

$$R = \frac{\lambda}{2NA} \tag{2.2}$$

where λ is the wavelength of electrons used and NA is the numerical aperture, which is engraved on each objective and condenser lens system, and a measure of the electron gathering ability of the objective, or the electron providing ability of the condenser [3].

2.2.2 Transmission electron microscopy (TEM)

In TEM, electrons are accelerated to 100 keV of higher (up to 1 MeV), projected onto a thin specimen (less than 200 nm) by means of the condenser lens system, and penetrate the sample thickness either undeflected or deflected. The greatest advantages that TEM offers are the high magnification ranging from 50 to 10^6 and its ability to provide both image and diffraction information from a single sample.

The scattering processes experienced by electrons during their passage through the specimen determine the kind of information

obtained. Elastic scattering involves no energy loss and gives rise to diffraction patterns. Inelastic interactions between primary electrons and sample electrons at heterogeneities such as grain boundaries, dislocations, second-phase particles, defects, density variations, etc., cause complex absorption and scattering effects, leading to a spatial variation in the intensity of the transmitted electrons. In TEM one can switch between imaging the sample and viewing its diffraction pattern by changing the strength of the intermediate lens.

The high magnification or resolution of all TEM is a result of the small effective electron wavelength, λ, which is given by the de Broglie relationship:

$$\lambda = \frac{h}{\sqrt{2mqV}} \tag{2.3}$$

where m and q are the electron mass and charge, h is Planck's constant, and V is the potential difference through which electrons are accelerated. For example, electrons of 100 KeV energy have wavelength of 0.37 nm and are capable of effectively transmitting through ~0.6 μm of silicon. The higher the operating voltage of a TEM instrument, the greater its lateral spatial resolution. The theoretical instrumental point-to-point resolution is proportional [4] to $\lambda^{3/4}$. High-voltage TEM instruments (with e.g. 400 KV) have point-to-point resolutions better than 0.2 nm. High-voltage TEM instruments have the additional advantage of greater electron penetration, because high-energy

electrons interact less strongly with matter than lower-energy electrons. So it is possible to work with thicker samples on a high-voltage TEM. One shortcoming of TEM is its limited depth resolution. Electron scattering information in a TEM image originates from a three-dimensional sample, but is projected onto a two-dimensional detector. Therefore, structure information along the electron beam direction is superimposed at the image plane. Although the most difficult aspect of the TEM technique is the preparation of samples, it is less so for materials.

2.2.3 Photoluminescence (PL)

Photoluminescence spectroscopy is a contactless, nondestructive method of probing the electronic structure of materials. Light is directed onto a sample, where it is absorbed and imparts excess energy into the material in a process called photo-excitation. One way this excess energy can be dissipated by the sample is through the emission of light, or luminescence. In the case of photo-excitation, this luminescence is called photoluminescence. The intensity and spectral content of this photoluminescence is a direct measure of various important material properties. The experimental setup for the PL measurements used in this study is schematically shown in Fig. 2.3.

Basically, it consists of an optical excitation light source, a

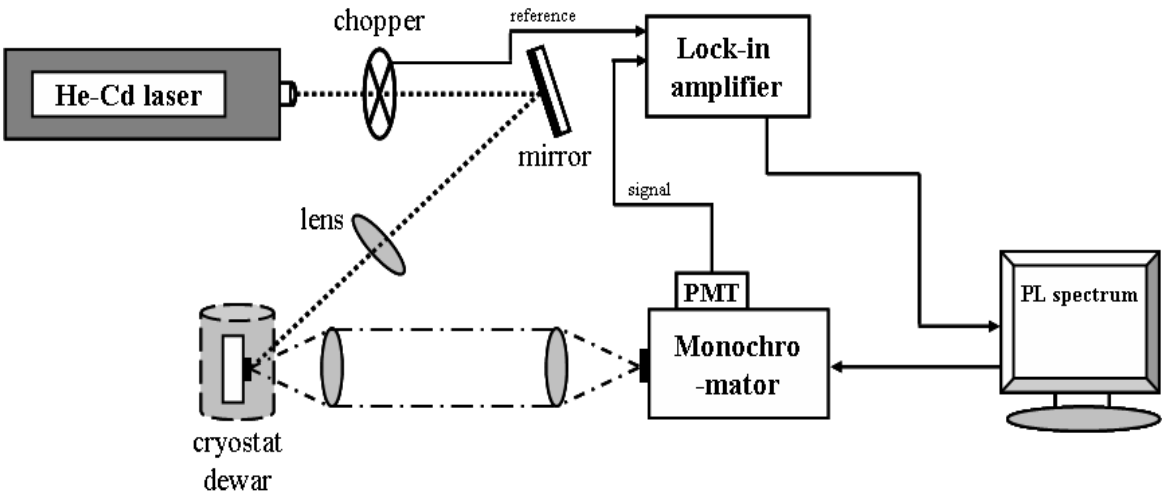

Fig. 2.3. Experimental setup used for PL measurements at low excitation.

spectrometer and a detector for the emitted light. For temperature dependence measurements, the temperature was controlled by a temperature controller and PL measurements were performed at temperatures of 300–10 K. PL spectra were measured using the 325 nm line of a He-Cd laser as an excitation source.

The major features that appear in a PL spectrum under low excitation are schematically shown in Fig. 2.4. In order of decreasing energy, the following structures are usually observed; CV, transition from the conduction band to the valence band; X, free excitons; D^oX and A^oX, excitons bound to neutral donors and acceptors, respectively; DV, transition from a donor to the valence band; CA, transition from the conduction band to an acceptor; DA, transition from a donor to an

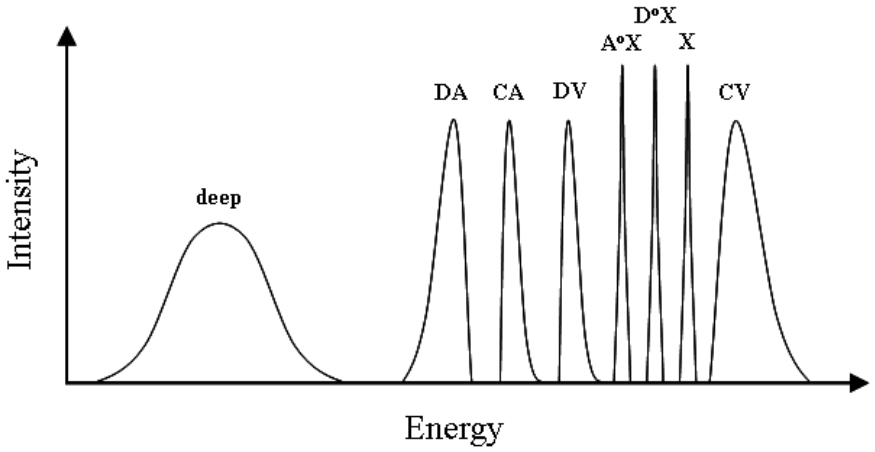

Fig. 2.4. Schematic representation of the major features in PL spectrum

acceptor; Deep, transition at deep state in the forbidden energy gap. All these recombination processes are represented schematically in Fig. 2.5.

The radiative transition from the condition band to the valence band is usually observed at temperatures higher than the dissociation energy of exciton (~100 K). The line shape is structureless and is given by an effective density of state term ($\sqrt{(h\nu - E_g)}$) multiplied by the Boltzmann filling factor [5]:

$$I_{CV} \propto \sqrt{(h\nu - E_g)} \exp\{-(h\nu - E_g)/k_B T)\} \qquad (2.4)$$

E_g is the energy gap of the semiconductor, $h\nu$ is the photon energy of the luminescence and k_BT has its usual meaning. It can be seen from equation (2.4) that the low energy edge of the structure gives the energy gap of the semiconductor and the temperature of carriers can

be obtained from the slope of the high energy part.

Recombination of electrons and holes through free excitons (X) takes place in a high-purity sample at low temperature. Bound excitonic emissions emerge in a near-gap luminescence spectrum as the donor or acceptor concentration is increased from a low level. A prominent type of recombination process involves the annihilation of an exciton bound to either of these species in their neutral charge state. The sensitivity of these sharp PL components to local strain in the sample may be exploited to reveal macroscopic built-in stress [6].

The recombination process from the conduction band to an acceptor state (CA) is free-to-bound transition. It can be seen from Fig. 2.5 that the low energy threshold of this CA transition can be described as in equation (2.4) for CV transition, but E_g must be replaced by $E_g - E_A$, where E_A is the position of the energy of the acceptor above the valence band edge. The CA luminescence band is mainly broadened by the kinetic energy of electrons before recombination.

The DA recombination processes compete strongly with the A^oX and D^oX transitions, especially when the concentration of donor and acceptor species is increased. The electronic interaction within the ionized donor-acceptor pair after the transition, as illustrated in Fig. 2.5, is responsible for the Coulomb term in the expression for the

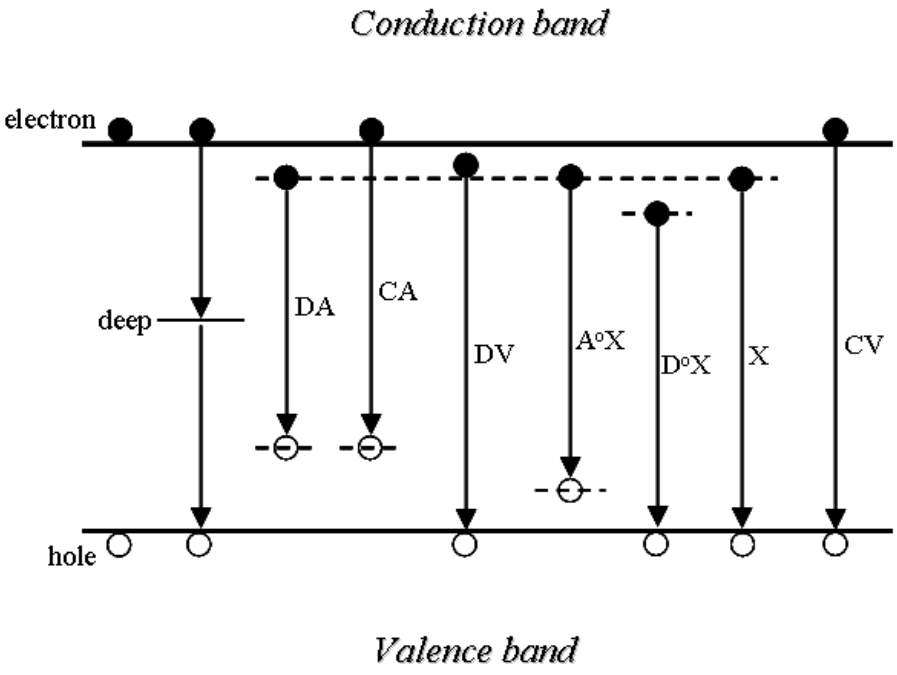

Fig. 2.5. Schematic representation of optical processes responsible for PL spectrum.

transition energy:

$$h\nu(\mathrm{DA}) = E_g - (E_A + E_D) + e^2/\varepsilon r \qquad (2.5)$$

where e is the elementary charge, r the separation of the donor-acceptor pair. The term $e^2/\varepsilon r$ in the equation (2.5) is responsible for the spectral dispersion into a very large number of discrete lines. Each line is associated with a different discrete value of r allowed by the lattice structure. But this discrete line structure is in most cases smeared out if lattice relaxation accompanies the electronic transition.

Many impurities and defects give rise to deep energy in the

forbidden energy gap of semiconductors. These deep states are efficient traps for excess carrier. Not only the capture process but also the resulting recombination through some of the deep centers are non radiative. However, other deep centers yield detectable emission bands. The knowledge about level luminescence is important, since it controls the minority carrier lifetime.

In general, nonradiative processes are associated with localized defect levels, whose presence is detrimental to material quality and subsequent device performance. Thus, material quality can be measured by quantifying the amount of radiative recombination.

2.2.4 High resolution X-ray diffraction (HRXRD)

Conventional high resolution X-ray diffraction (HRXRD) has been developed as a powerful tool for the non-destructive ex-situ investigation of materials. The information, which is obtained from diffraction patterns, concerns the composition and uniformity of an epitaxial layer, its thickness, the built-in strain and strain relaxation, and the crystalline perfection related to its dislocation density. The principal setup is shown in Fig. 2.6. It combines a four-crystal monochromator and a multiple-reflection analyzer crystal to perform high-resolution measurements for reciprocal lattice scans. A Ge(220) 4-crystal monochromator added by the crossed slit attachment is used

as an x-ray beam source. The Ge 4-crystal monochromator produces a beam with very low divergence and small wavelength spread. The crossed slit collimator is designed to provide a point x-ray source. The slit is variable in width up to 10 mm with a step of 0.02 mm. The diffraction beam is detected by a double arm attachment which is used for high resolution application. One arm is a rocking curve attachment and the second arm carries the channel cut analyzer crystal to convert to a triple axis mode.

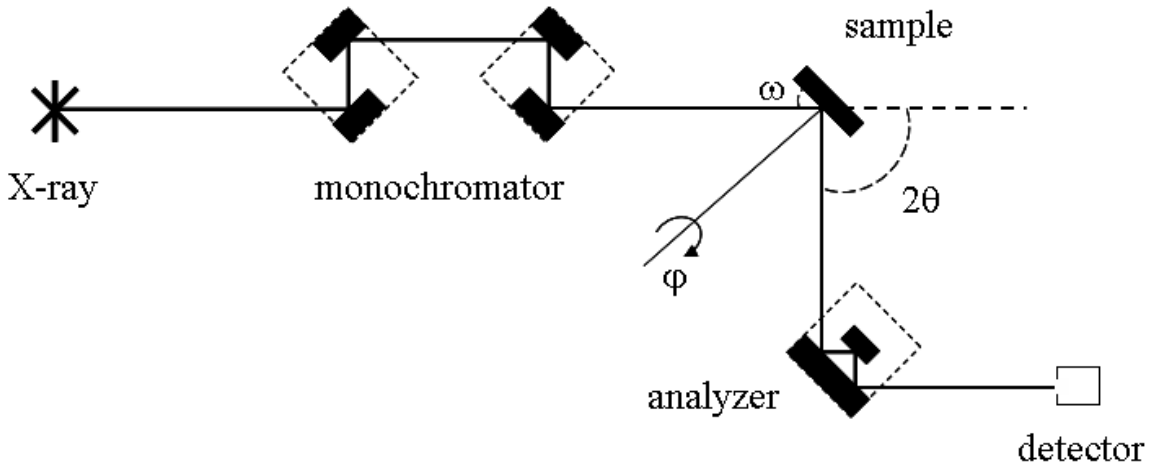

Fig. 2.6. The geometry of the high resolution four crystal eight reflection diffractometer.

Fig. 2.7 shows the scan directions for data collection. Diffractometer angles consist of the ω angle between the incident beam and sample surface, the 2θ angle between incident beam and detector, the ψ sample tilt about the axis in the diffraction plan, and the ϕ

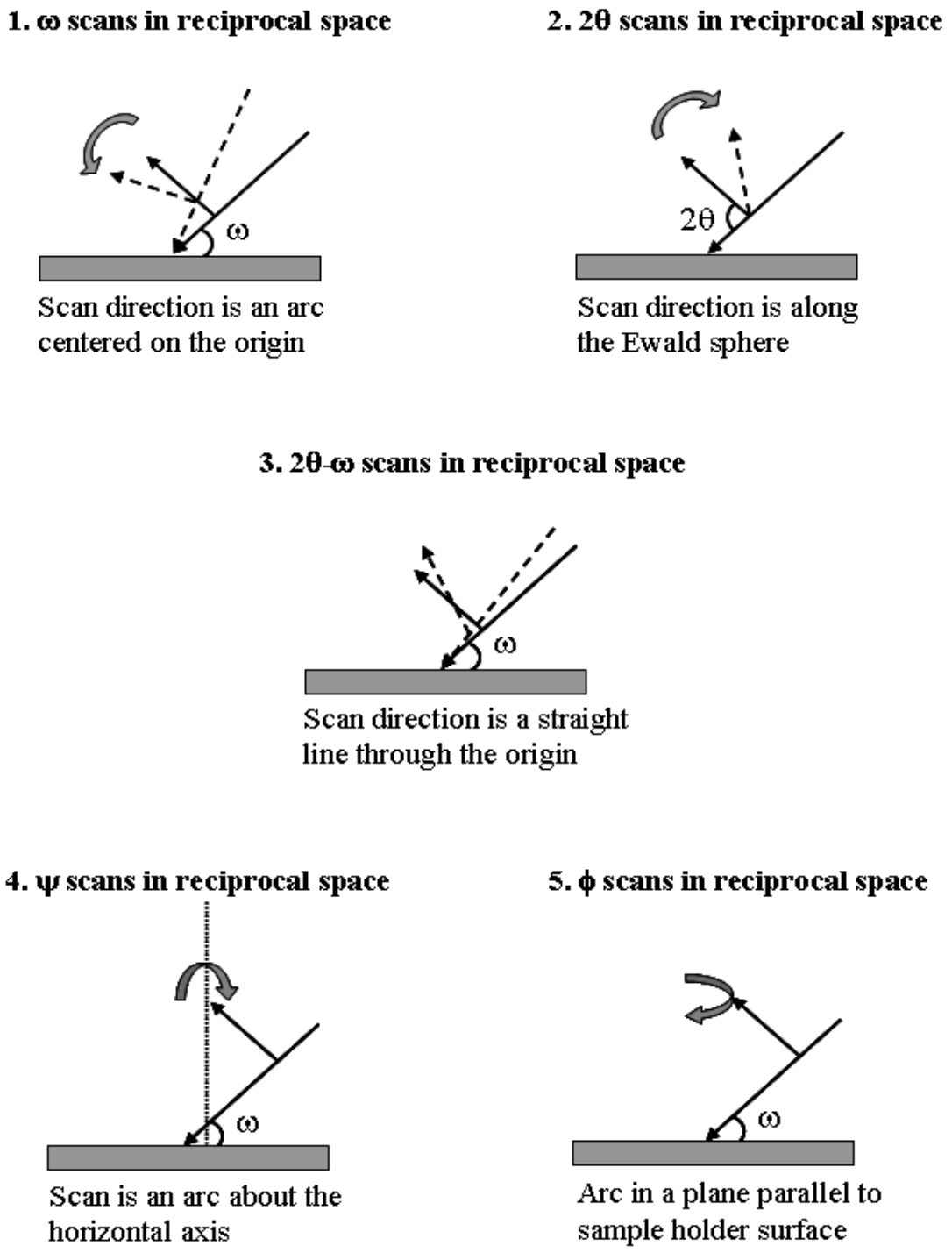

Fig. 2.7. Scan directions for data collection in a HRXRD system. Diffractometer angles consist of the ω angle between the incident beam and sample surface, 2θ angle between the incident beam and detector, ψ sample tilt about the axis in a diffraction plane, and ϕ rotation about the sample normal.

rotation about the sample normal. The scan direction of the ω scan is an arc center on the origin, that of the 2θ scan is along the Ewald sphere, that of the $2\theta-\omega$ scan is a straight line through the origin, that of the ψ scan is an arc along the horizontal axis, and that of the ϕ scan is an arc in a plane parallel to the sample holder surface.

In this research, the $2\theta-\omega$ scan and the ω scan are mainly used. In the case of the $2\theta-\omega$ scan which makes the detector rotate twice as faster as the sample rotation around the diffractometer axis, the head of the scattering vector moves along the direction of the scattering vetor in reciprocal space during scan. In the ω scan, the detector position is fixed, while the sample is rotated around the diffractometer axis. The head of the scattering vetor moves perpendicular to the scattering vector in reciprocal space.

REFERENCES

[1] E.I. Givargizov, *Highly Anisotropic Crystals*, Dordencht (1986)

[2] R.S. Wagner, *Whisker Technology*, Wiley (1970)

[3] Guozhong Cao, *Nanostructures & Nanomaterials*, Imperial College Press (2004)

[4] M. von Heimendahl, *Electron Microscopy of Materals: An Introduce*, Academic Press (1980)

[5] D.J. As, L. Palmetshofer, *J. Appl. Phys.* 62 (1987) 369

[6] P.J. Dean, C.H. Henry, C.J. Frosch, *Phys. Rev.* 168 (1968) 812

Chapter 3. Catalytic growth of ZnO nanorods on AuGe catalyst

3.1 Introduction

Nanostructures exhibit peculiar and fascinating properties compared with their bulk counterparts. In nanostructures, the density of states of carriers is concentrated to a certain levels of energy, which enables enhancement of exciton oscillator strength and light-emitting efficiency. As a result, the performance of nanostructure-based optical devices is expected to be improved and to be less temperature dependent [1].

One-dimensional (1D) nanostructure materials, such as nanotubes, nanowires and nanobelts have attracted much attention because of their interesting properties for understanding fundamental physical concepts and for potential applications [2-6]. Among the wide variety of 1D semiconductor nanostructures, ZnO nanorods attract special interest for optoelectronic nano-devices due to the simple structural configuration. In the last few years, several methods including metalorganic chemical vapor deposition (MOCVD), physical vapor deposition (PVD) and vapor phase transport (VPT) have been employed to synthesize 1D ZnO nanostructures [7-10]. Among these methods, VPT with a catalyst is the simplest and widely used method, which provides an unique advantage that is the controllability of

nanostructure.

In this chapter, it is proposed to use new binary material as a catalyst for nanostructure growth. Since the melting point and the vapor pressure of alloys strongly depend on alloy composition, alloy catalysts are expected to have many advantages in compare to elemental ones in terms of size- and density- controllability. Moreover, it has been seldom studied on this catalyst as far as we concerned.

In the growth using catalyst, synthesis is carried out on the basis of the vapor-liquid-solid (VLS) growth mode. In VLS growth of ZnO nanorods, a liquid droplet of an alloy forms on substrate at the temperature predicted from the phase diagram of zinc and catalytic metal system. The source materials containing Zn are preferentially absorbed on liquid droplets due to higher sticking coefficient of Zn on liquid versus solid. When the concentration of Zn supersaturate in the droplet, Zn begins to precipitate at the interface between droplet and substrate and forms the rod structure.

In this chapter, we report on the growth of well-aligned 1D ZnO nanorods by vapor phase transport method using AuGe as a new catalyst. The growth conditions were systematically investigated and the feasibility of this new catalyst is examined in terms of the uniformity and high optical quality of nanorods.

3.2 Experimental

ZnO nanorods were grown by vapor-phase transportation process. First of all, a thin layer of AuGe was deposited on SiO_2/Si substrates. When the horizontal quartz tube furnace reached to the expected temperature from 600 ^oC to 700 ^oC, a quartz tray was inserted into the quartz tube furnace for the nanostructure growth. AuGe-coated substrate and zinc powders (5N) were placed on the same tray. After 30 min. growth, the tray was drawn out from the quartz tube furnace and cooled down to room temperature. Dry N_2 was used as a carrier gas, and flows through the quartz tube during the growth with the flow rate of 500 (ml/min.). The morphologies and structures of the synthesized samples were analyzed by scanning electron microscopy (SEM) and high resolution X-ray diffraction (HRXRD). The photoluminescence (PL) spectroscopy was used to evaluate the optical property of the samples at room temperature. And a He-Cd (325 nm) laser was used as an excitation source.

3.3 ZnO nanostructure by growth temperatures

AuGe catalyst (7 wt.% Ge) was deposited by thermal evaporation on the SiO_2/Si substrates. Typical thickness of AuGe layer was controlled to about 50 nm. The melting temperature of this catalyst is known as 660 ^oC, which is much lower than that of Au (1064 ^oC) [11].

Although there might be many parameters that affect the formation of nanostructures, the growth temperature determines the vapor pressure of Zn

and thermodynamic processes. Therefore, it is generally believed as the most important parameter for nanostructure formation. The conventional model to explain the growth mechanism of 1D structure involves the participation of VLS in the growth process. The central idea of the VLS growth can be divided into two stages: 1) the nucleation and growth of eutectic alloy droplets and 2) the growth of nanorods through the liquid droplets due to supersaturation. During the growth process, the catalyst absorbs the vapor components such as Zn (vapor) and Zn_xO ($x<1$, vapor), to form a eutectic alloy. When it is supersaturated, crystallization of ZnO will occur [12]. It should be pointed out that if the ambient temperature of this process is too high, oxygen vaporization will be accelerated and the nanostructure tends to contain a lot of oxygen deficiencies. Various reports support this description, generally at high growth temperature the degradation of optical property and forfeit of uniformity are observed [13]. In this experiment, therefore, the growth temperature is restricted to 700 ^{o}C considerably lower than that for Au-catalyzed VPT method.

Fig. 1 shows SEM images of three different nanostructures, which were grown at different temperatures. Fig. 1 (a) is the morphology of the sample grown at 600 ^{o}C, which shows several thick pillars along with islands-like structures with hexagonal facets on the top surface. While, Fig. 1 (b) shows nanorods grown at 650 ^{o}C (150 ± 5 nm in diameter and 8 ± 0.5 μm in length). Finally, Fig. 1 (c) (grown at 700 ^{o}C) shows high-density long needle like

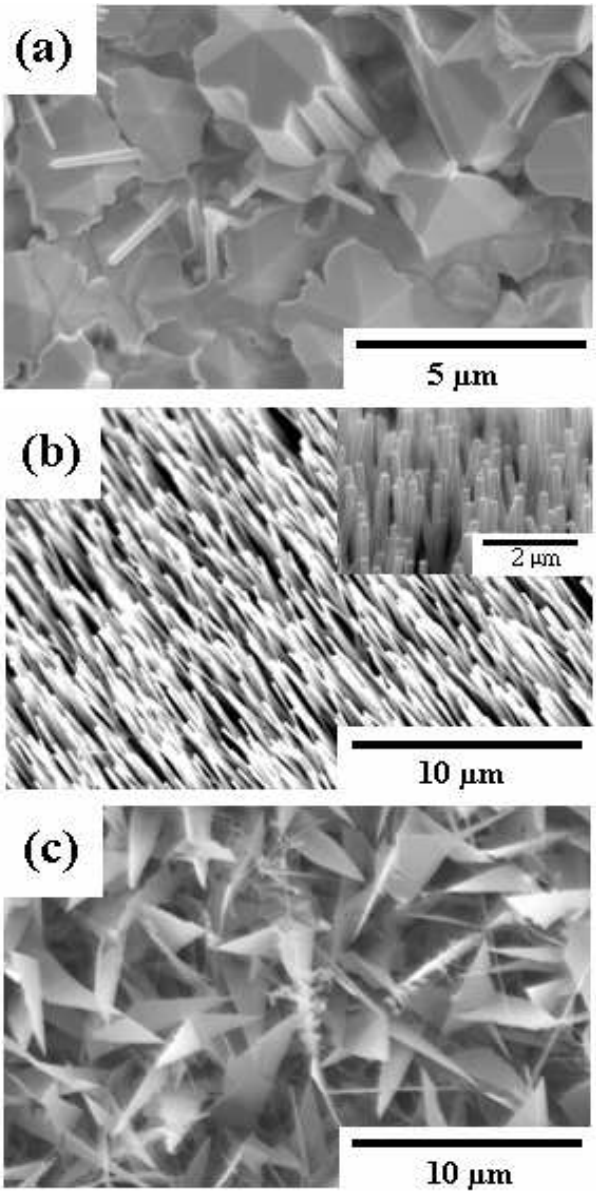

Fig. 3.1. SEM images of ZnO nanostructures. (a) ZnO pillars and islands grown at 600 ^{o}C, (b) uniform ZnO nanorods obtained at 650 ^{o}C and (c) ZnO wire with sheets formed at 700 ^{o}C.

nanowires and the triangular sheets between nanowires, which is usually regarded as a proof of second-phase growth [14].

Fig. 1 (a) can be considered as the result of spatially simultaneous

growth due to low solubility of AuGe at the low growth temperature (600 ^{o}C). While, in the case of the sample shown in Fig. 1 (b), increase of solubility makes the dispersion of solute concentration in the solution, which results in the spatial distribution of initial nuclei. Once crystallization starts from an nuclei, growth in the c-axis direction will be preferred due to high surface energy of c-plane. Resultantly rod-like structures are formed. However, when we increase the growth temperature up to 700 ^{o}C (Fig. 1 (c)), the dimension of nuclei will shrink due to the increase of solubility, accordingly slender wire-type structures appear. Moreover, the second phase growth will be promoted as shown in Fig. 1 (c), due to the increase of Zn and Zn_xO vapor supply.

It is interesting to note that the variation of diameters of rod-type structures. First of all, the diameter of ZnO pillar observed in the Fig. 1 (a) is in micrometer scale as large as 2.5 μm, however it becomes nanometer scale structure as the growth temperature increases with the diameter of ~ 150 nm, and it finally becomes needle-like structure with a diameter of ~ 90 nm at the highest temperature. These results can be understood in terms of the temperature dependence of nuclei size as explained above.

3.4 The optical properties

Fig. 2 shows room temperature PL spectra of the samples grown at (a) 600 ^{o}C, (b) 650 ^{o}C and (c) 700 ^{o}C, respectively. All samples show strong UV

emission with negligible deep level emission. The UV emission centered at 3.243 eV is assigned as a near band edge excitonic emission. Fig.2 (a) shows relatively weak UV emission intensity but the green emission is not observed. When the growth temperature increases to 650 ^{o}C, the UV emission intensity increases, but green emission is not observed, too. While the growth temperature increases further up to 700 ^{o}C, green emission appears, although UV emission intensity also increases.

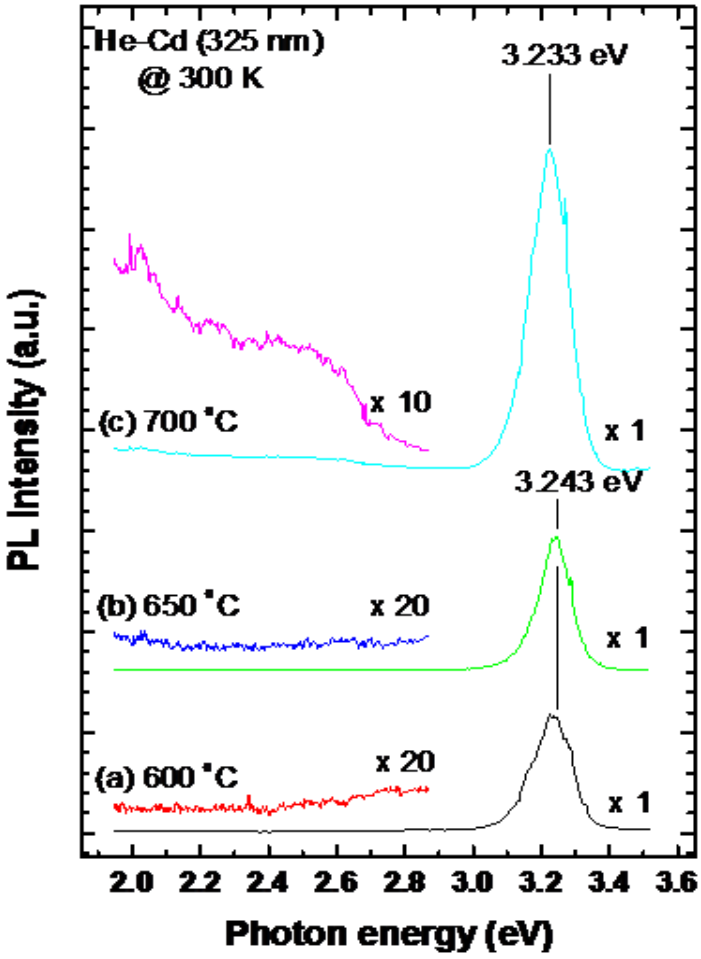

Fig. 3.2. PL spectra of the samples grown at (a) 600 ^{o}C, (b) 650 ^{o}C and (c) 700 ^{o}C, measured at room temperature.

Note that, the increase of the absolute PL intensity does not simply mean the excellence of optical property. Generally, not the absolute PL intensity but the relative intensity ratio of I_{UV} to $I_{green\text{-}band}$ is connected to the crystal quality of nanostructures [15]. Therefore, nanorod structures are considered to have the best optical quality in our experiment. Also, these results indicate the predominance of a low temperature growth, because in the case of Au catalyzed ZnO nanorods grown at higher temperatures (700 ~ 950 ^{o}C) usually show strong green emission at around 2.45 eV [16,17]. This fact also strongly supports the usefulness of alloy catalyst because the formation of oxygen vacancy is enhanced at high temperature. Similar discussion is also possible, based on the previous report [18]. In the report, nevertheless oxygen atmosphere, the green emission intensity increased by annealing, and eventually it dominates the PL spectrum at 850 ^{o}C. Hence, it is considered that the decrease of growth temperature is really useful to diminish the oxygen vacancy generation.

3.5 Divergence of nanorods

Fig. 3 shows (a) the histogram of tilting angle estimated from SEM image, (b) the high resolution X-ray diffraction (HRXRD) measurement 2-dimensional mapping result of ZnO nanorods grown at 650 ^{o}C. The tilting angle is assessed to be as ± 5.5 degree. It is well known that the linewidth of X-ray rocking curve reveals the mosaicity of crystal such as tilting, twisting

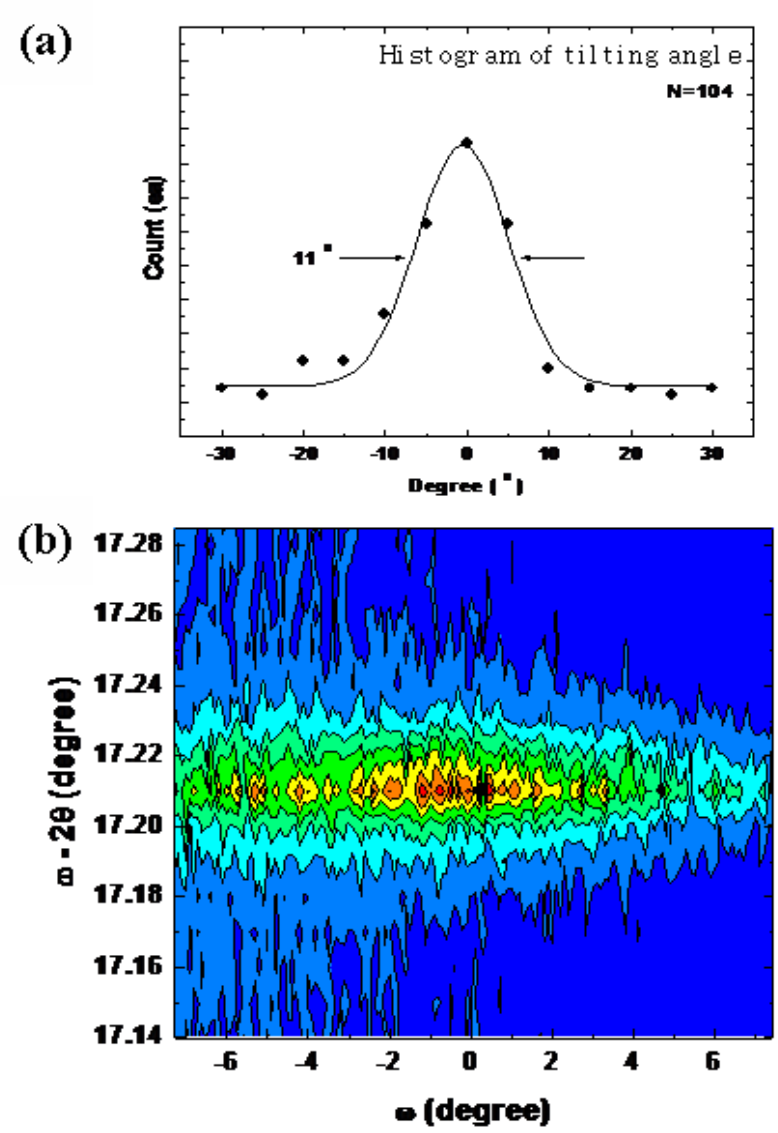

Fig. 3.3. Structural uniformity of the nanorods estimated by SEM and HRXRD. (a) The histogram of tilting angles of ZnO nanorods grown at 650 ^{o}C and (b) a reciprocal space mapping of ZnO nanorods grown on AuGe-coated substrate.

and bending. The tilting of nanorods can be estimated by the omega linewidth broadening, since, this value represents the deviation of c-axis direction. As shown in Fig. 3 (b), the full width at half maximum (FWHM) of omega scan

is evaluated as ~ 11.9 degree, which corresponds well with the tilting angle estimated from SEM image.

Also, the linewidth of ω-2θ scan is as wide as 0.014 degree. The linewidth of ω-2θ reflects inhomogeneous strain and/or the disorder of reflection plane spacing. In our experiment, it is tentatively assumed that inhomogeneous strain from the bending of nanorods is responsible for the observed broadening based on the SEM observation.

3.6 Summary

As a new catalyst, which confirms both controllable growth and high crystallinity of ZnO nanorods, AuGe is introduced. ZnO nanostructures were grown by simple vapor transportation method in a function of growth temperature. All samples show high optical quality with strong UV emission and negligible deep level emission. It is discussed that the low growth temperature due to the low melting temperature of AuGe is really useful to diminish the defect generation. Also 2D HRXRD mapping result is analyzed by using the statistical treatment of SEM result. We define the uniformity of the nanorods in terms of narrow FWHM of ω-2θ scan and the small divergence of tilting angle. In conclusion it is shown that AuGe is a good candidate as a new catalyst for ZnO nanostructures, which confirms high crystal quality of the nanostructure.

REFERENCES

[1] Y. Arakawa and H. Sasaki, *Appl. Phys. Lett.* 40 (1982) 939

[2] Y.J. Xing, Z.H. Xi, and Z.Q. Xue, *Appl. Phys. Lett.* 83 (2003) 1689

[3] M.H. Huang, Y. Wu, and H. Feick, *Adv. Mater.* 13 (2001) 113

[4] X.Y. Kong and Z.L. Wang, *Appl. Phys. Lett.* 84 (2004) 975

[5] W.L. Hughes and Z.L. Wang, *J. Am. Chem. Soc.* 126 (2004) 6703

[6] Z.L. Wang, X.Y. Kong and J.M. Zuo, *Phys. Rev. Lett.* 91 (2003) 185502

[7] J.J. Wu and S.C. Liu, *Adv. Mater.* 14 (2002) 215

[8] Y.C. Kong, D.P. Yu, and B. Zhang, *Appl. Phys. Lett.* 78 (2001) 407

[9] C.X. Xu, X.W. Sun, and B.J. Chen, *Chem. Phys. Lett.* 20 (2003) 1319

[10] C.X. Xu, X.W. Sun, and B.J. Chen, *J. Appl. Phys.* 95 (2004) 661

[11] H. Okamoto and T.B. Massalski, *Phase Diagrams of Binary Gold Alloys* (1987)

[12] E. McGlynn, J. Grabowska, and K.K. Nanda, *Sur. & Coat. Tech.* 200 (2005) 1093

[13] C. Andreazza, P. Andreazza and D. Zhao, *Superlatt. and Microstruct.* 39 (2006) 340

[14] Y.X. Chen, M. Lewis and W.L. Zhou, *J. Cryst. Growth* 282 (2005) 85

[15] B.D. Yao, Y.F. Chen and N. Wang, *Appl. Phys. Lett.* 81 (2002) 757

[16] N.E. Hsu, W.K. Hung and Y.F. Chen, *J. Appl. Phys.* 96 (2004) 4671

[17] J. Park, H.H. Choi, and K. Siebein, *J. Cryst. Growth* 258 (2003) 342

[18] X.Q. Meng, D.Z. Shen, and J.Y. Zhang, *Solid State Commun.* 135 (2005) 179

Chapter 4. Growth of well-aligned ZnO nanorods on ITO glass

4.1 Introduction

Nanoscale one-dimensional (1D) materials have stimulated great interest due to their importance in basic scientific research and potential technological allocations [1,2]. Other than carbon nanotubes, 1D nanostructure such as nanowires or quantum wires are ideal system for investigating the dependence of electrical transport, optical and mechanical properties on size and dimensionality. They are expected to play an important role as both interconnects and functional components in the fabrication of nanoscale electronic and optoelectronic devices. Many unique and fascinating properties have already been proposed, or demonstrated for this class of materials such as superior mechanical toughness [3], higher luminescence efficiency [4], enhancement of thermoelectric figure of merit [5], and a lowered lasing threshold [6]. Among the wide variety of 1D semiconductor nanostructures, ZnO nanorods attract special interest for optoelectronic nano-devices due to the simple structural configuration. ZnO has been recognized as one of the promising photonic materials in the ultraviolet region [7] because of its wide direct band gap (3.37 eV, at RT) and large exciton binding energy (60 meV). Some interesting optical properties, for

example room-temperature ultraviolet laser emission, in ZnO nanostructureshave been demonstrated.

In this experiment, it is proposed to use indium-tin-oxide (ITO) glass as a substrate for nanorod growth. The carrier concentration of highly conducting ITO films is in the range of 10^{20}-10^{21} atoms/cm^3. Furthermore, ITO is a wide band gap semiconductor (E_g: 3.5-4.3 eV, the gap between the CB and VB where no wavelike electrons obital exist), which shows high transmission in the visible [8-10]. Due to these properties, ITO has been used in a wide range of applications.

In this chapter, report on the growth of well-aligned ZnO nanorods on ITO glass by simple vertical vapor phase transportation (V-VPT) method. It was focused on the evaluation of the effects of two important growth parameter such as growth temperature and carrier gas flow. In addition, the growth parameter was studied through systematic growth temperature.

4.2 Experimental

ZnO nanorods were grown on ITO glass by vertical vapor phase transportation (V-VPT) method without any assistance of catalyst. The growth temperature and N_2 gas flow were controlled each other by experimental conditions. First of all, prepared the ITO coated about 75 nm on glass substrates were cleaned with organic solvents. When the horizontal quartz tube furnace reached to growth temperature a quartz tray was inserted

into the quartz tube furnace for the nanostructure growth. ITO-coated glass and zinc powders were placed on the same tray. After 30 min. growth, the tray was drawn out from the quartz tube furnace and cooled down to room temperature. In first experimental, the growth temperature was controlled from 500 ^{o}C to 650 ^{o}C and Dry $N_2$was used as a carrier gas, and flows through the quartz tube during the growth with the flow 600 (ml/min). In second experiment, N_2 gas flow was controlled from 500 (ml/min) to 800 (ml/min) with the growth temperature fixed 650 ^{o}C. The morphologies and structures of the synthesized samples were analyzed by scanning electron microscopy (SEM). The photoluminescence (PL) spectroscopy was used to evaluate the optical property of the samples at room temperature. And a He-Cd (325 nm) laser was used as an excitation source.

4.3 Growth processes of ZnO nanorods via VL growth method

The morphology of ZnO grown on ITO glass by vapor-phase-transportation (VPT) method was investigated. Growth temperature was controlled from 500 ^{o}C to 650 ^{o}C. Fig. 4.1 show the growth process of ZnO nanorods and Fig. 4.2 is plan-view images and cross section images by SEM.

Generally growth temperature is an important parameter for growth mechanism of nanostructure. ZnO nanostructures with various growth condition have been studied using growth temperature [7,11], growth time [12], substrate [13], source [14], catalyst [15-19]. Particularly, the growth

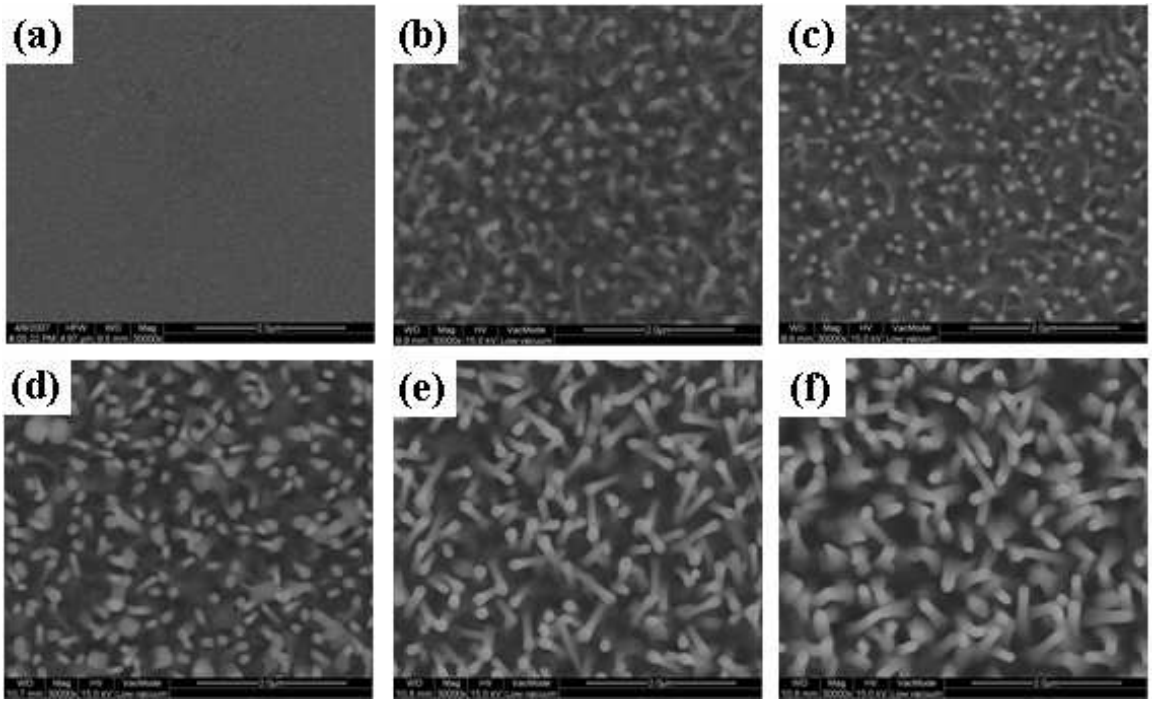

Fig. 4.1 SEM images of ZnO nanorods grown on ITO glass at (a) 500 ^{o}C, (b) 550 ^{o}C, (c) 575 ^{o}C, (d) 600 ^{o}C, (e) 625 ^{o}C and (f) 650 ^{o}C.

temperature has strong influence on the shape and quality of nanostructure and plays an important role for the formation.

Fig. 4.2 shows cross section images of ZnO nanorods in different growth temperature. The growth process of ZnO nanorods was successfully obtained through control of systematic growth temperature. On the basis of these observations, we propose that the growth of ZnO nanorods may occur via a VS process [20,21]. We suggest that the process proceeds as follows: First, Zn vapor is generated by thermal evaporation of Zn powder and transported to substrate surface, where the in coming Zn vapor is preferentially adsorbed on the ITO layer. With the increase of the Zn

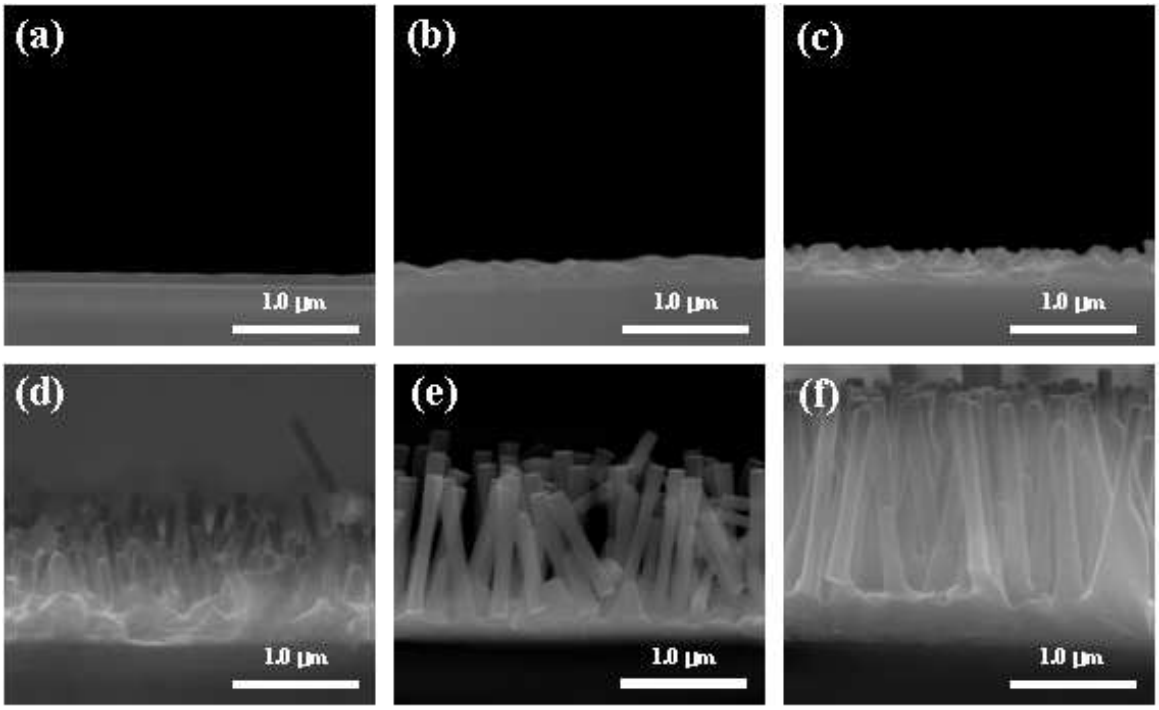

Fig. 4.2. Cross section images of ZnO nanorods grown on ITO glass at (a) 500 ^{o}C, (b) 550 ^{o}C, (c) 575 ^{o}C, (d) 600 ^{o}C, (e) 625 ^{o}C and (f) 650 ^{o}C.

concentration, instead of precipitating zinc and zinc-phase buffer layers are formed on the substrate in the form of either ITO-Zn-O alloy or zinc oxide. Subsequently, the rough nature of the large island on the fissured ZnO buffer layers serves as energetically preferred absorption sites for the incoming vapor Zn, for condensation and nucleation. As the Zn vapor continues to be deposited onto these nucleation sites, it is immediately oxidized, and nanorods are formed through a VS process.

4.4 Various features of ZnO nanorods by growth parameters

Fig. 4.3 shows the variation of length, dispersion angle, diameter and

density of ZnO nanorods according to controllable growth parameter such as growth temperature and carrier gas flow. In Fig. 4.3 (a), ZnO nanorods were grown at different growth temperature and N_2 carrier gas flow was fixed on 600 ml/min. As the growth temperature increasing, length was increased and dispersion angle was decreased. When the growth temperature increases to 600 ^{o}C, diameter was decreased and, density was increased. Above 600 ^{o}C, diameter was increased and, density was decreased. In Fig. 4.3 (b), ZnO nanorods were grown on changed carrier gas flow and growth temperature was fixed at 650 ^{o}C. As the carrier gas flow increasing, length and dispersion

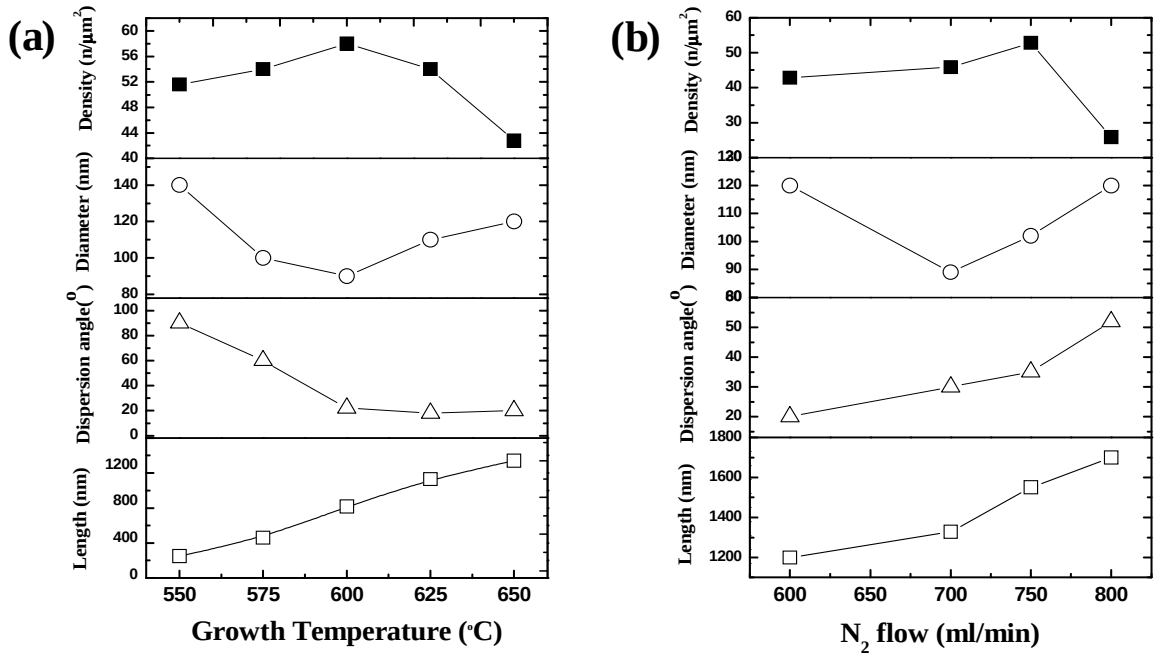

Fig. 4.3. Numerical values of length, dispersion angle, diameter and density of ZnO nanorods according to controllable growth parameter such as (a) growth temperature and (b) carrier gas flow.

angle was increased. While the carrier gas flow further up to 700 ml/min diameter was decreased but over 700 ml/min carrier gas flow increased diameter. When the carrier gas flow increases to 750 ml/min density was increased, and then density was decreased.

From these results, one can find that not only the growth temperature but also carrier gas flow has a great influence in the formation of ZnO nanorods. Length of ZnO nanorods increased according to increasing the growth

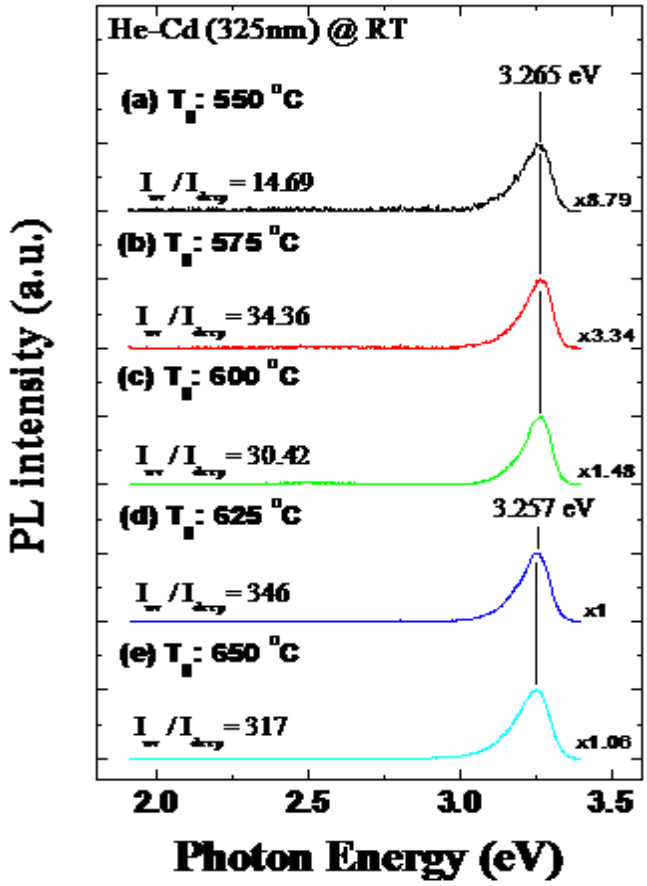

Fig. 4.4 PL spectra of the samples grown at (a) 550 ^{o}C, (b) 575 ^{o}C, (c) 600 ^{o}C, (d) 625 ^{o}C and (e) 650 ^{o}C. , , measured at room temperature.

temperature and carrier gas flow. This might be explained by thermodynamics. Under the high growth temperature and the heavy gas flow, evaporation pressure of Zn increases, which icreases the length of rods. In case of dispersion angle, as growth temperature increasing well-aligned ZnO nanorods could be obtained. On the other hand, dispersion angle was increased as carrier gas flow increasing.

4.5 Optical properties

Fig. 4.4 shows room temperature PL spectra, taken from the ZnO nanorods grown at (a) 550 ^{o}C, (b) 575 ^{o}C, (c) 600 ^{o}C, (d) 625 ^{o}C and (e) 650 ^{o}C, respectively. All samples show strong UV emission with negligible deep level emission. The UV emission centered at 3.257 eV is assigned as a near band edge (NBE) excitonic emission. When the growth temperature increases to 625 ^{o}C the UV emission intensity increases, but green emission weakens. While the growth temperature increases further up to 625 ^{o}C, the intensity ratio (UV emission/green emission) was increased.

4.6 Summary

Well-aligned ZnO nanorods were grown on ITO glass by vertical vapor phase transportation (V-VPT) method. Growth temperature and carrier gas flow were varied in the wide ranges and various features of ZnO nanorod were compared by growth parameter. The growth parameter was discussed

through controlled growth temperature. All samples show high optical quality with strong UV emission and negligible deep level emission.

REFERENCES

[1] J. Hu, T.W. Odom, C.M. Lieber, *Ass. Chem. Res.* 32 (1999) 435

[2] Y. Wu, H. Yan, P. Yang, *Chem. Eur. J.* 8 (2002) 1260

[3] E.W. Wang, P.E. Sheehan, C.M. Lieber, *Science* 277 (1997) 1971

[4] J.D. Holmes, K.P. Johnston, R.C. Doty, B.A. Korgel, *Science* 287 (2000) 1471

[5] L.D. Hicks, M.S. Dresselhaus, *Phys. Rev.* B 47 (1996) 16631

[6] M. Huang, S. Mao, H. Feick, H. Yan, Y. Wu, H. Kind, E. Weber, R. Russo, P. Yang, *Science* 292 (2001) 1897

[7] B.D. Yao, Y.F. Chan and N. Wang, *Appl. Phy. Lett.* 81 (2002) 757

[8] Z.W. Yang, S.H. Han, T.L. Yang, Lina Ye, and C.F. Cheng, *Thin solid films* 366 (2000) 4

[9] Y.S. Kim, Y.C. Park, S.G. Ansari, and H.S. Shin, *Surface and Coatings Technology* 173 (2003) 299

[10] S.H. Keshmiri, M. Rezaee-Roknabadi, S. Ashok, *Thin solid films* 413 (2000) 167

[11] Z. Chen, N. Wu, Z. Shan, and S.X. Mao, *Scripta. Mater.* 52 (2005) 63

[12] W.I. Park, D.H. Kim, S.W. Jung, G.C. Yi, *Appl. Phy. Lett.* 80 (2002) 4232

[13] T. Yashi, M. Yasuda, and D. Nezaki, *Thin Solid Films* 464-465 (2004) 273

[14] Y.H. Leung A.B. Djurisic, and J. Gao, *Chem. Phys. Lett.* 385 (2004) 155

[15] C.J. Lee, T.J. Lee, S.C. Lyu, and Y. Zhang, *Appl. Phy. Lett.* 81 (2002) 3648

[16] M.H. Huang, Y. Wu, and H. Feick, *Adv. Mater.* 13 (2001) 113

[17] H.T. Ng, J. Li, and M.K. Smith, *Science* 300 (2003) 1249

[18] S.Y. Li, C.Y. Lee, T.Y. Tseng, *J. Cryst. Growth* 247 (2003) 357

[19] S.C. Lyu, Y. Zhang, and H. Ruh, *Chem. Phys. Lett.* 363 (2002) 134

[20] Z.W. Pan, Z.R. Dai, Z.L. Wang, *Science* 291 (2001) 1947

[21] P.D. Yang, C.M. Lieber, *J. Mater. Res.* 12 (1997) 2981

Chapter 5. ZnO nanorod device using sandwiched Si-substrates

5.1 Introduction

Wide-bandgap materials are under intensive studies to improve the responsivity and stability of UV photodetectors [1-3]. Among them, ZnO is of great interest due to its strong UV photoresponse, well-established synthesis methods, and the capability of operating at high temperature and harsh environments [4-6].

One-dimensional (1D) nanostructures have attracted much attention because of their interesting properties and various potential applications [7,8]. Among them, ZnO nanorods (NRs) attract special interest for optoelectronic nano-devices due to the simple structural configuration. Also simple and well-defined vapor phase transportation (VPT) method been developed, and provides a unique advantage that is the controllability of nanostructure [9].

Electrical and optical properties of nanostructures are typically measured by making metallic contacts to NRs placed on an insulating substrate. To fabricate such devices NRs are usually separated from a substrate on which the NRs were initially grown and then are randomly dispersed onto a desired insulating substrate after being diluted in a solution. Also complicated processes are required to contacting the NRs with a measurement system.

Although this approach is suitable for the investigation of physical properties of NRs, it is time- and cost-consuming process.

A possible approach to solve this problem is direct lateral growth of NRs between two adjacent electrodes. Recently, similar idea was successfully realized using etched Si substrates without any assistance of catalyst [10]. This method can be applied to various applications, also may provide the simplest way of fabricating nano-device and measuring the electrical properties of nanostructures. Although sometimes catalyst hinder the performance of device [11], it is helpful for the synthesis of various nanostructures in terms of the size, position, density control of the nanostructures. We were trying to use the benefits of the catalyst and one-step synthesis of nanorod in between the two adjacent Si substrates, simultaneously.

In this chapter, we present a direct NR growth by using a sandwiched Si substrate. Various metals were pre-deposited on the Si-substrates and the growth of NRs on it was optimized. We also demonstrated that the device fabricated by using this method shows good current-voltage and photoresponse properties.

5.2 Experimental

ZnO nanorods were grown by vapor-phase transportation process. First of all, various metal layers (Sn, AuGe, Al, Ag, Au, Ni, and Ti) with various

physical properties (melting points, crystal structures, lattice constants) were deposited by thermal evaporator and e-beam evaporator on Si substrates.

The NR growth was started from the inserting of a quartz tray into the quartz tube furnace at 650 ^{o}C. Metal-deposited Si substrate and zinc powder were placed on the same tray. After 30 min. growth, the tray was drawn out from the quartz tube furnace and cooled down to room temperature. Dry N_2 was used as a carrier gas, and flows through the quartz tube during the growth with the flow rate of 500 (ml/min.).

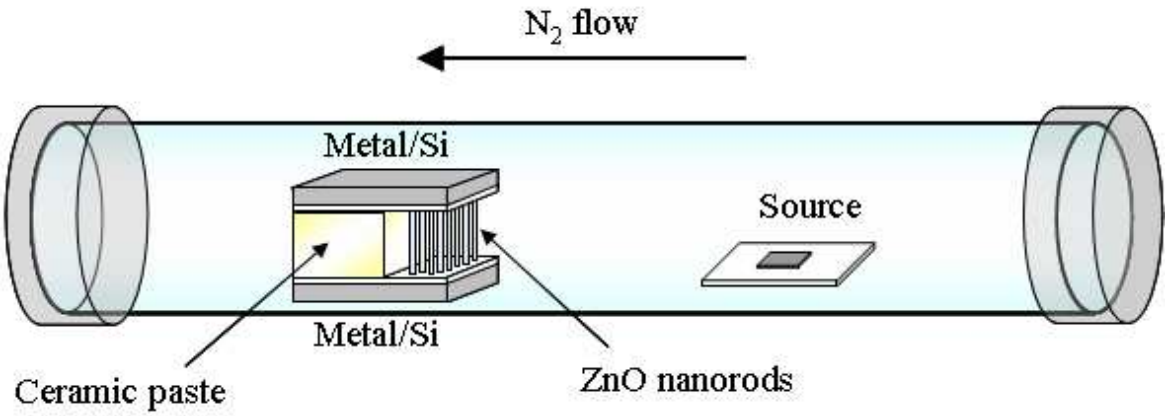

Fig. 5.1. Schematic of ZnO nanorod growing across the metal deposition Si substrate.

Fig. 5.1 shows how to fabricate the sandwiched Si-substrate. The sandwiched Si-substrates were made as follows; (1) Pre-deposition of metals on each Si substrate. (2) Glue the Si substrates together with ceramic paste, in this process the metal deposited surface should be faced, but be insulated each other. The distance between substrates was 6 μm. (3) Position the

sandwiched Si-substrates at the fixed position in a sample tray with Zn-source. The growth condition of NRs in between the two parallel Si-substrates was just the same as that of the NRs growth itself.

The morphologies and structures of the synthesized samples were analyzed by scanning electron microscopy (SEM) and transmission electron microscopy (TEM). The photoluminescence (PL) spectroscopy was used to observe the optical property of the NRs at room temperature. Electronic properties and photoresponse spectrum were obtained by current-voltage (*I*–*V*) characteristics curve and photocurrent, respectively. For the photoresponse measurement Xe lamp with the output power of 500 W was used as a white light source and the spectrum was not normalized.

5.3 ZnO nanorods on various metal catalysts

Fig. 5.2 shows SEM images of ZnO nanorods on different metal catalysts. Fig. 5.2 (a) is the morphology of the sample grown on AuGe thin film, which shows vertically well-aligned ZnO nanorods. Mean diameters and lengths of the nanorods were in the range of 155-165 nm and 5-6 μm, respectively. Fig. 5.2 (b) have revealed needle-like nanorods and sheet-like morphologies. The synthesized ZnO nanorods on Al thin film were typically about 30-40 nm in diameter and 1-2 μm in length. Fig. 5.2 (c) present an image of ZnO nanorods grown on Ag thin film with 30-40 nm diameter and 850-900 nm length. Fig. 5.2 (d) shows the ZnO nanorods based on Au layer.

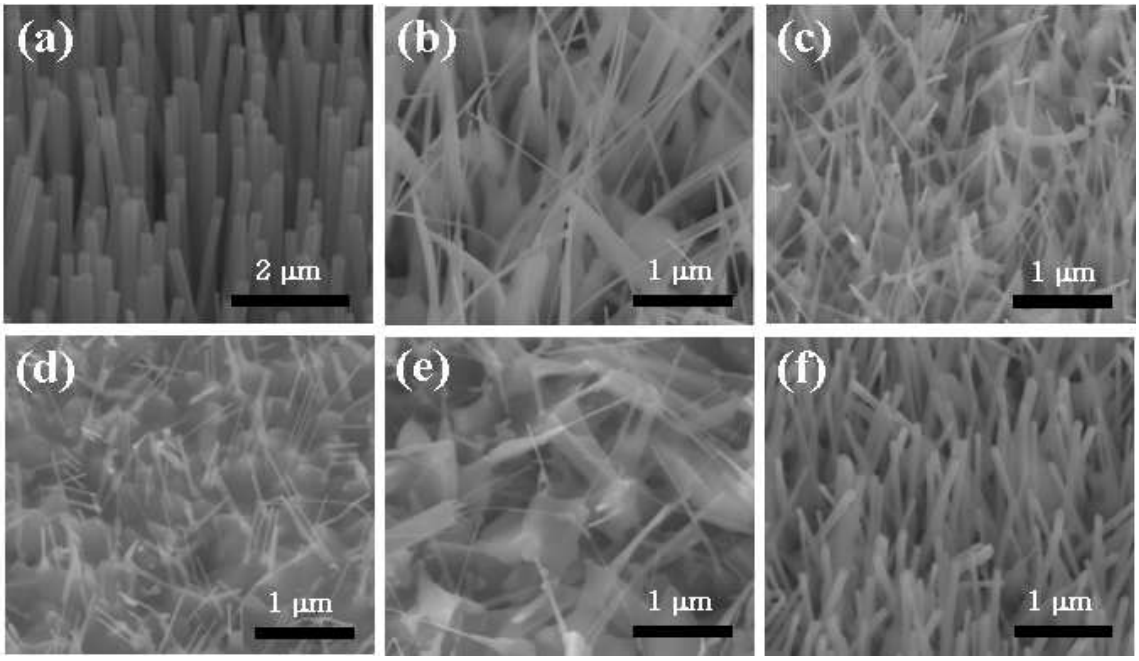

Fig. 5.2. Field-emission scanning electron microscopy (FE-SEM) images of ZnO nanorod growth on SiO_2/Si substrate using various metal catalysts. (a) ZnO nanorod (diameter: 155-165 nm) using AuGe metal, (b) ZnO nanorod (diameter: 30-40 nm) using Al metal, (c) ZnO nanorod (diameter: 30-40 nm) using Ag metal, (d) ZnO nanorod (diameter: 20-30 nm) using Au metal, (e) ZnO nanorod (diameter: 15-20 nm) using Ni metal, (f) ZnO nanorod (diameter: 60-70 nm) using Ti metal.

Note that surface appears to be covered by a thin buffer layer formed prior to the nanorod growth, most probably due to AuZn oxides. Diameter and length were in the range of 20-30 nm and 70-80 nm, respectively. Fig. 5.2 (e) shows long needle-like nanorods and the webbing-like sheets between nanowires, which is usually regarded as a proof of second-phase growth [12]. ZnO nanorods on the Ni thin film have 15-20 nm diameters and 900-910 nm length. Finally Fig. 5.2 (f) exhibits ZnO nanorods grown on thin-deposited

layer. The synthesized ZnO nanorods were in the range of 60-70 nm in diameter and in the range of 2-3 μm in the length.

In Fig. 5.2, we described the growth of ZnO nanorods using the various catalytic metals. Generally melting temperature, surface energy and crystal structure of metal catalyst are influence on nanostructure formation. These are believed as the important parameter for growth mechanism of nanostructure. Melting temperatures and materials properties of the used metals were exhibited in table 5.1.

Table 5.1 Material properties of metal catalysts

	Melting point [^{o}C]	Crystal structure	Lattice parameter [Å]
Sn	231.9	Diamond	a:6.49
AuGe	660	Hexagonal	4.08 – 5.658
Al	660.1	fcc	a:4.05
Ag	960.8	fcc	a:4.09
Au	1063	fcc	a:4.08
Ni	1453	fcc	a:3.52
Ti	1668	Hexagonal (hcp)	a:2.95 b:4.68

5.4 Well-aligned ZnO nanorods

Fig. 5.3 shows SEM images of ZnO nanorods on metal catalyst layers which show vertically well-aligned ZnO nanorods. Fig. 5.3 (a) is the morphology of the sample grown on AuGe thin film. The tilting angle is

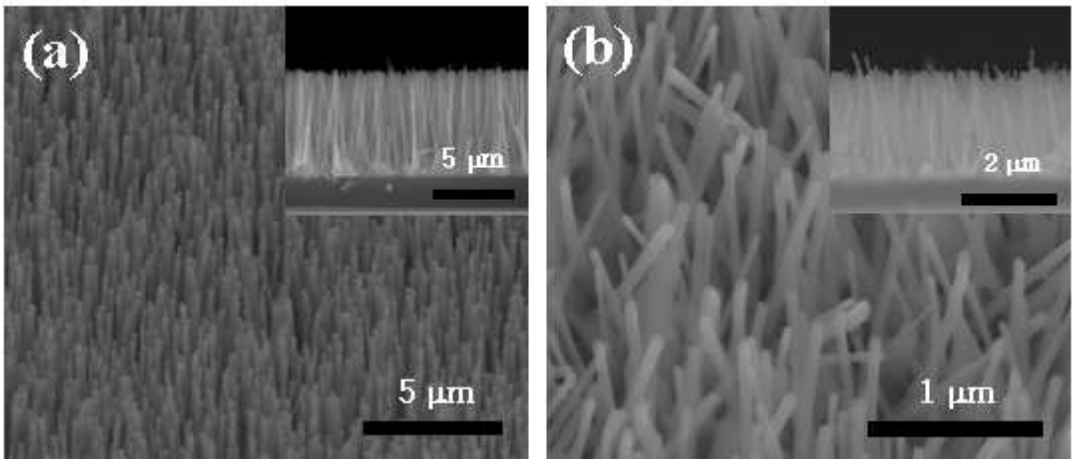

Fig. 5.3. Tilted-view SEM images show a mean divergence of ZnO nanorods. The insets show typical cross-sectional images. A mean divergence of ZnO nanorod is (a) 3 ^{o} on AuGe tin film metal and is (b) 5.5 ^{o} on Ti thin film.

assessed to be as ± 3 ^{o} degree. Fig. 5.3(b) exhibits ZnO nanorods grown on Ti thin film. The synthesized ZnO nanorods were in the range ± 3 ^{o} degree in divergence.

On the basis of these observations, we propose that for the metal thin film catalysts, the growth of ZnO nanorods may occur via a VS process [13,14]. We suggest that the process proceeds as follows: First, Zn vapor is generated by thermal evaporation of Zn powder and transported to substrate surface, where the incoming Zn vapor is preferentially adsorbed on the large metal islands formed at 650 ^{o}C. With the increase of the Zn concentration, instead of precipitating zinc, zinc-phase buffer layers are formed on the substrate in the form of either metal-Zn-O alloy or zinc oxide. Subsequently, the rough nature of the large islands on the fissured ZnO buffer layers serves

as energetically preferred absorption sites for the incoming vapor Zn, for condensation and nucleation. As the Zn vapor continues to be deposited onto these nucleation sites, it is immediately oxidized, and nanorods are formed through a VS process. Finally, it is worth pointing out the noble-metal catalysts may result in the difference in nanorod growth mode for noble-metal catalysts.

5.5 The growth mechanism of ZnO nanorods

Fig. 5.4 shows SEM images of ZnO nanorods on three different metal catalysts. Fig. 5.4 (a) is the morphology of the sample grown on Sn thin film. The inset image shows SEM image of a thin nanorod with an alloy tip. The presence of the alloy tip is an indication of the conventional VLS growth mechanism. Fig. 5.4 (b) and Fig. 5.4 (c) exhibits ZnO nanorods grown on AuGe thin filmand Al thin films, respectively. The inset image shows TEM image of a thin nanorod without an alloy tip.

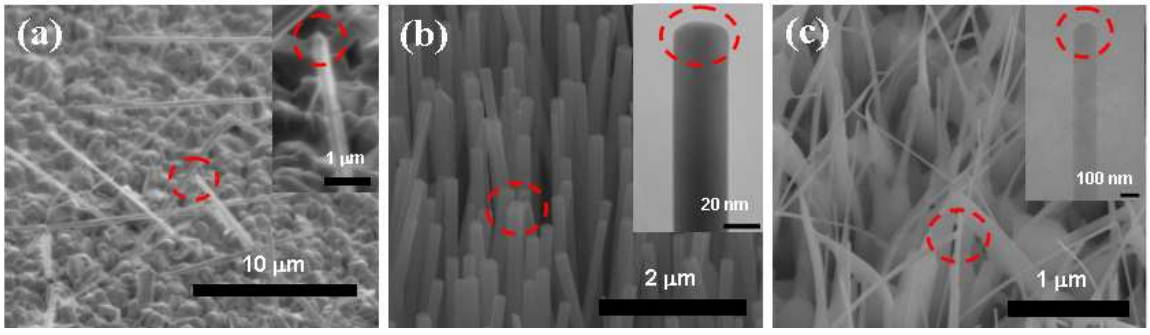

Fig. 5.4. SEM images of ZnO nanorod on (a) Sn, (b) AuGe and (c) Al metal layers. The insets show TEM images of ZnO nanorods on their tip.

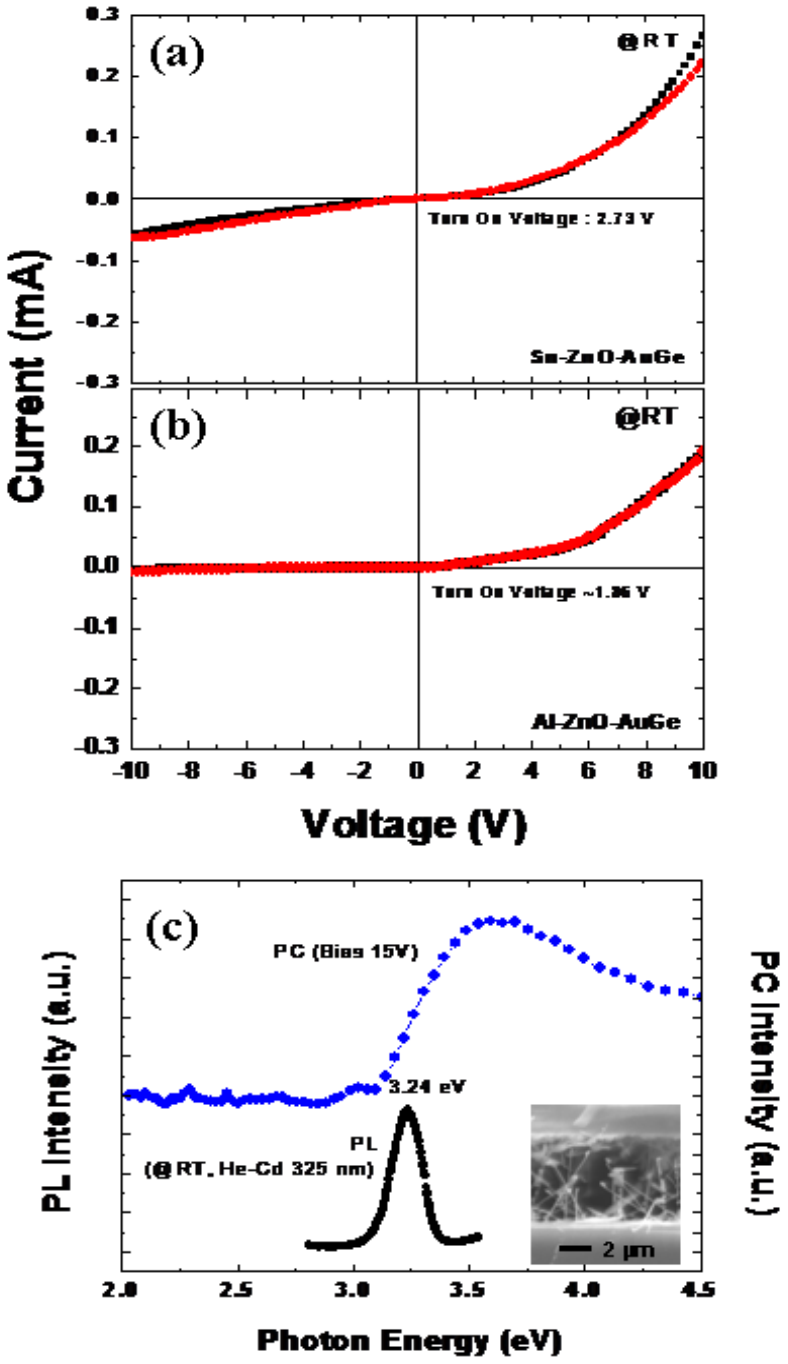

Fig. 5.5. (a) Typical (*I–V*) characteristic curve of Sn-ZnO-AuGe diode and (b) Al-ZnO-AuGe dide. (c) Photocurrent spectrum of the nanorods: PL spectrum taken for the nanorods is added. Inset: SEM image of ZnO nanorods formed between Sn and AuGe.

5.6 Electrical properties of ZnO nanorod device

Shown in fig. 5.5 are the (*I–V*) characteristics and photocurrent of ZnO metal-semiconductor-metal circular devices. Fig. 5.5 (a) shows a typical (*I–V*) characteristic curve measured on Sn-ZnO-AuGe diode. As shown in Fig. 5.5 (a), the (*I–V*) characteristic curve shows a turn-on voltage of ~2.73 V for the forward bias and a reverse bias breakdown voltage of -4.3 V. Fig. 5.5 (b) shows a typical (*I–V*) characteristic curve measured on Al-ZnO-AuGe diode, exhibiting clear rectifying behavior without significant reverse-bias breakdown up to 10 V. this significantly enhanced (*I–V*) characteristic curve was routinely obtained. Fig. 5.5 (c) shows photocurrent spectrum of the Sn-ZnO-AuGe diode under the modulated illumination of photon energy ranging from 2.0 eV to 4.5 eV; for comparison PL spectrum taken for the nanorods is added in this figure. In the PL spectrum, the strong free-exciton peak is present. In spite of the presence of the free-exciton PL peak, the excitonic band is absent in the photocurrent spectrum. This observation implies that excitons excited by the above gap light in the ZnO nanorods do not contribute to the photoconduction, but that the excitons participate in the recombination to emit the PL signal.

5.7 Summary

The ZnO nanorods on various metal layer grown and fabricated Shottky diode using ZnO nanorods has been investigated electrical characteristics. It

is discussed that the growth mechanisms using various metal catalysts by several parameters. Al-ZnO-AuGe Schottky diodes obtained better electrical characteristic. The sensitivity to UV emission (3.24 eV) was confirmed using Sn-ZnO-AuGe Schottky diode. In conclusion it is shown that Sn-ZnO-AuGe Shottky diode is an excellent possibility as a UV detector.

REFERENCES

[1] N. Biyikli, O. Aytur, I. Kimukin, T. Tut, E. Ozbay, *Appl. Phys. Lett.* 81 (2002) 3272

[2] M.L. Lee, J.K. Sheu, W.C. Lai, S.J. Chang, Y.K. Su, M.G. Chen, C.J. Kao, G.C. Chi, J.M. Tsai, *Appl. Phys. Lett.* 82 (2003) 2913

[3] A. Bouhdada, M. Hanzaz, F. Vigue, J.P. Faurie, *Appl. Phys. Lett.* 83 (2003) 171

[4] S. Liang, H. Sheng, Y. Liy, Z. Huo, Y. Lu, H. Shen, *J. Cryst. Growth* 225 (2001) 110

[5] I.S. Jeong, J.H. Kim, S. Im, *Appl. Phys. Lett.* 83 (2003) 2946

[6] S.J. Pearton, D.P. Norton, K. Ip, Y.W. Heo, T. Steiner, *J. Vac. Sci. Technol. B* 22 (2004) 932

[7] W.L. Hughes and Z.L. Wang, *J. Am. Chem. Soc.* 126 (2004) 6703

[8] Z.L. Wang, X.Y. Kong and J.M. Zuo, *Phys. Rev. Lett.* 91 (2003) 185502

[9] B.D. Yao, Y.F. Chen, N. Wang, *Appl. Phys. Lett.* 81 (2002) 757

[10] J.S. Lee, M.S. Islamand S. Kim, *Nano Lett.* 6(7) (2006) 1487

[11] W.I. Park, D.H. Kim, S.W. Jung and G.C. Yi, *Appl. Phys. Lett.* 80 (2002) 4232

[12] Y.X. Chen, M. Lewis and W.L. Zhou, *J. Cryst. Growth* 282 (2005) 85

[13] Z.W. Pan, Z.R. Dai, Z.L. Wang, *Science* 291 (2001) 1947

[14] P.D. Yang, C.M. Lieber, *J. Mater. Res.* 12 (1997) 2981

Chapter 6. Conclusions

Nanotechnology is a new field or a new scientific domain. Similar to quantum mechanics, on nanometer scale, materials or structures may possess new physical properties or exhibit new physical phenomena. Some of these properties are already known. For example, band gaps of semiconductors can be tuned by varying material dimension. These may be many more unique physical properties not known to us yet. These new physical properties or phenomena will not only satisfy everlasting human curiosity, but also promise new advancement in technology. Nanotechnology also promises the possibility of creating nanostructures of metastable phases with non-conventional properties including superconductivity and magnetism. Yet another very important aspect of nanotechnology is the miniaturization of current and new instruments, sensors and machines that will greatly impact the world we live in.

Nanostructures offer an extremely broad range of potential applications from electronics, optical communications and biological systems to new materials. Many possible applications have been explored and many devices and systems have been studied. In this thesis, one-dimensional well-aligned ZnO nanorods were grown by

vapor-phase-transfortation (VPT) method for the application to UV detector. In order to achieve this purpose, we have systematically studied.

First of all, optimum growth conditions are obtained using novel catalyst, AuGe, through controlled growth temperature in chapter 3. As a new catalyst, which confirms both controllable growth and high crystallinity of ZnO nanorods, AuGe is introduced. All samples show high optical quality with strong UV emission and negligible deep level emission from PL spectra. High structural quality with narrow FWHM of ω-2θ scan along and small divergence of tilting angle were demonstrated from HRXRD result and SEM image.

And then the growth mechanism of ZnO nanorods grown on ITO glass were investigated from controlled growth parameters in chapter 4. Growth temperature and carrier gas flow were varied in the wide ranges and various features of ZnO nanorod were compared using results. PL spectra show higher UV intensity with increasing growth temperature caused by increasing surface-to- volume ratio.

Finally, feasibility of application as an UV detector was demonstrated in chapter 5. The ZnO nanorods on various metal layer grown and fabricated Shottky diode using ZnO nanorods has been investigated electrical characteristics. It is discussed that the growth mechanisms using various metal catalysts by several parameters.

Al-ZnO-AuGe Schottky diodes obtained better electrical characteristic. The sensitivity to UV emission (3.24 eV) was confirmed using Sn-ZnO-AuGe Schottky diode. In conclusion it is shown that Sn-ZnO-AuGe Shottky diode is an excellent possibility as a UV detector.

APPENDIX I.

Hard x-ray photoemission spectroscopy (HX-PES)

Photoemission spectroscopy (PES) has been used extensively to determine core level and valence band electronic structure [1]. It utilizes the photoelectric effect in which an electron is ejected from the occupied electronic levels of the sample. In a conventional PES experiment, the kinetic energy of the photoelectrons usually varies from a few electron volts up to a few hundred electron volts, depending on the photon energy used. Thus this technique is surface sensitive, as the inelastic mean free paths (IMFPs) of typical photoelectrons in a solid are in the range of 0.5-3 nm. This means that ultra high vacuum (UHV) is necessary to maintain a surface free of adsorbates during the time scale of the measurement, and that the surface effect should be considered during the interpretation of the resulting spectra.

In this section, the instrument, special features, and efficiency of hard x-ray photoemission spectroscopy by using brilliant synchrotron radiation in SPring-8 are introduced. Also possible research using the dimension of the probe depth is described.

A.1.1 Advantages of the hard x-ray excitation

Up to now, PES has been considered a surface sensitive method

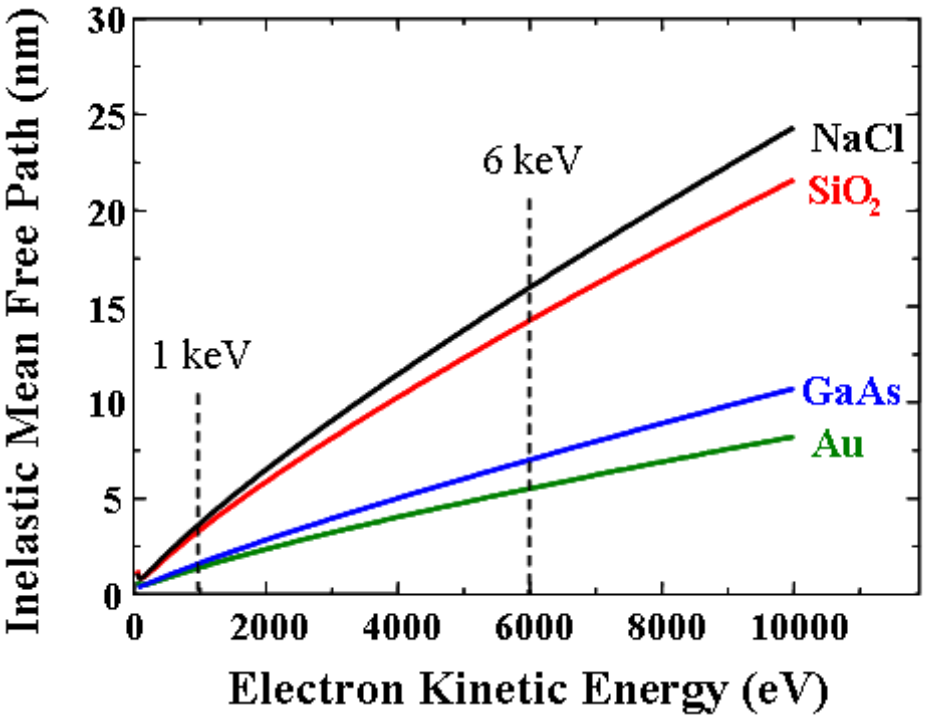

Fig. A.1.1. Inelastic mean free paths for electron kinetic energies up to 10 keV, for Au, GaAs, SiO_2 and NaCl.

because of the short IMFPs due to low kinetic energies as described in Fig. A.1.1 In order to attain longer probing depths than that in vacuum ultraviolet (VUV) spectroscopy, soft x-ray PES using synchrotron radiation has recently become attractive [2]. However, it is obvious that soft x-ray PES is still surface sensitive, because the IMFPs of a valence electron are only 1.3 and 2 nm for Au and Si at a kinetic energy of 1 keV, respectively [3]. It should be noted that if surface reconstruction occurs, which is often the case for semiconductors, the depth of the surface extends down to around 1 nm. In contrast to the surface sensitive PES techniques, the IMFPs values of a valence electron for Au and Si increase to 5.5 and 9.2 nm, respectively, at 6

keV [4], which lies in the range of hard x-ray. The larger probing depth results in small surface contributions. The first feasibility test of hard x-ray PES was done by Lindau *et al*. [4] in 1974 using a first generation synchrotron radiation source. However, the feeble signal intensity of even the Au 4*f* core level spectrum excluded the possibility of valence band studies. What has prohibited hard x-ray valence band PES is the rapid decrease in atomic subshell photoionization cross section (σ) as shown in Fig. A.1.2 [5].

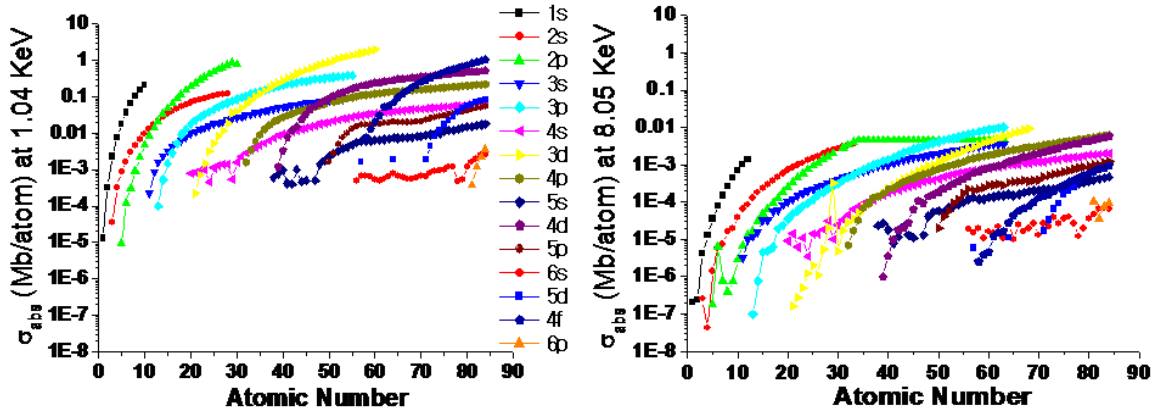

Fig. A.1.2. Plots of atomic subshell photoionization cross sections at 1.04 keV (right) and 8.05 keV (left) for the elements (Z=1 to 85).

The σ values for Au 5*d* (1×10^{-5} Mb) and Si 3*p* (3×10^{-5} Mb) at 6 keV are only 1 ~ 2 % of those at 1 keV [1]. However, hard x-ray PES with high throughput and resolution has been realized by using the third generation high energy synchrotron at SPring-8. Unprecedented high photon flux and flux density from an undulator [6,7] compensate for the decrease in cross section and make hard x-ray valence band PES possible.

A.1.2 Experimental setup

A schematic of the experimental setup including optics is shown in Fig. A.1.3. X-ray monochromatized at 5.95 keV with a Si (111) double crystal monochromator were vertically focused with a cylindrically bent mirror onto samples mounted in an analyzer chamber. A channel-cut monochromator with a Si (333) reflection placed downstream of the mirror made it possible to reduce the energy bandwidth to 70 meV. At the sample position, a photon flux in a focal spot of 0.12 mm (vertical) × 0.7 mm (horizontal) was measured at 2×10^{11} counts/s. In order for easy operation, the sample manipulator is motorized and CCD cameras are attached. The vacuum of the analyzer chamber was 10^{-4}-10^{-5} Pa during measurements. No surface treatment was carried out and all the samples were investigated as inserted.

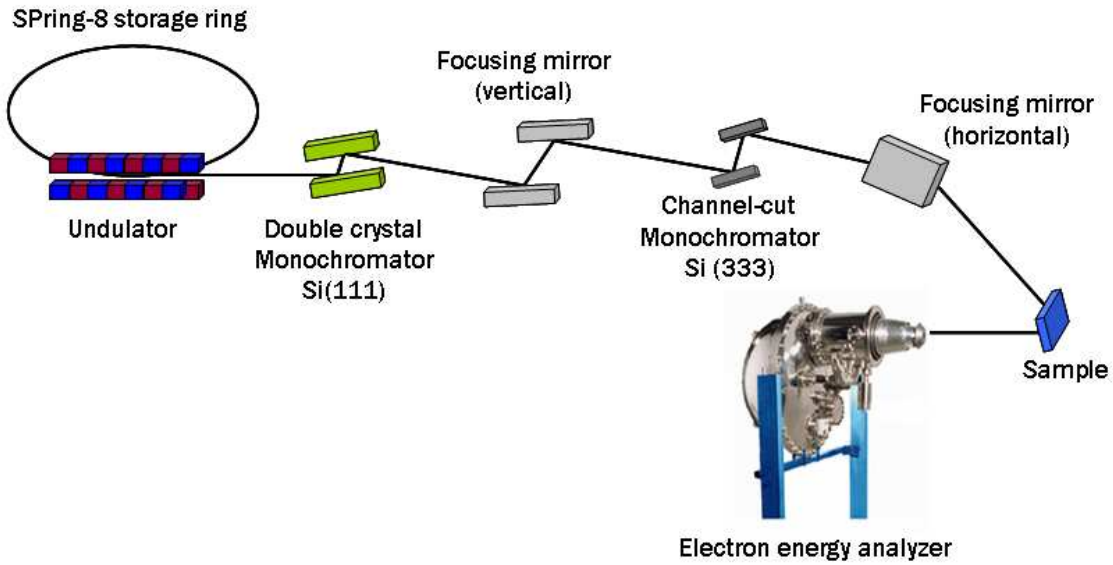

Fig. A.1.3. Schematic of hard x-ray PES experimental setup including optics.

REFERENCES

[1] S. Hufner, *Photoelectron Spectroscopy*, Springer (1995)

[2] The electron inelastic mean-free-paths were estimated using NIST Standard Reference Database 71, "NIST Electron Inelastic-Mean-Free-Path Database: Ver 1.1" It is distributed via the web site *http://www.nist.gov/srd/nisthtm*, and reference therin

[3] A. Sekiyama, T. Iwasaki, K. Matsuda, Y. Saitoh, and S. Suga, *Nature* 403 (2000) 396

[4] I. Lindau, P. Pianetta, S. Doniach, and W.E. Spicer, *Nature* 250 (1974) 214

[5] J.J. Yeh and I. Lindau, *At. Data Nucl. Data Tables* 32 (1985) 1

[6] H. Kitamura, *Rev. Sci. Instrum.* 66 (1995) 2007

[7] H. Kitamura, *J. Synchrotron Radiat.* 7 (2000) 121

감사의 글

졸업논문을 마무리하며 그 동안의 시간들을 떠올려봅니다. 나열 할 수 없을 만큼의 많은 일들이 있었고 저에게도 많은 변화가 있었습니다. 그 중심에는 언제나 저의 지도교수님이신 장지호 교수님이 계셨습니다. 교수님의 가르침 말로 다 할 수 없지만, 졸업논문의 한켠을 빌려 감히 감사의 말씀드립니다. 지난 3년간 교수님의 곁에서 배울 수 있었던 것이 저에게는 너무도 큰 행운이었고 행복이었습니다. 언제나 교수님의 가르침을 떠올리며 부끄럽지 않은 제자가 되도록 노력하겠습니다. 아울러 반도체물리전공의 훌륭하신 교수님들, 이삼녕 교수님, 안형수 교수님, 양민 교수님, 김홍승 교수님 그동안의 가르침에 진심으로 감사드립니다. 그리고 고항주 박사님, 오동철 교수님, 이홍찬 교수님의 조언에 깊은 감사드립니다.

매사 꼼꼼하게 챙겨주시는 이봉춘 조교님, 실험동 선배 경화언니, 주영언니, 은수언니, 대현선배, 명훈선배, 근숙언니께 감사드립니다. 그 동안 많은 것 챙겨주시고, 도움 주셔서 정말 감사합니다. 오랜 시간 함께 한 재현언니, 실험동의 헌수오빠, 충현오빠, 상현오빠, 인혜에게도 고마운 마음 전하고 싶습니다.

우리연구실의 첫 선배이신 승환선배, 3년간 저의 투정을 받아주시고 언제나 옆에서 든든한 힘이 되어주신 미나언니께 진심으로 감사드립니다. 부족한 후배 이뻐해주시고 이끌어주셔서 정말 감사합니다. 연구실은 떠났지만 언제나 응원을 보내주는 광희선배, 진우선배, 규범오빠, 현경이에게도 고마운 마음 전합니다. 언제나 씩씩한 웅오빠, 든든한 동기 시영이, 승준이, 상냥한 성국오빠, 이제 막 연구생 생활을 시작한 시내, 지은이, 미연이에게 고마운 마음 전합니다. 이분들과 함께 한 모든 시간들이 소중했고 오랜시간 동안 잊지 못할 것입니다. 언제까지나 고민하고 발전하는 우리연구실이 될 것이라 믿어 의심치 않습니다.

일본에 있는 동안 저의 보호자(?)를 자청해주신 김박사님과 혜지언니, 맛있는 음식, 좋은 곳 찾아다니며 많은 추억 만들어 주신 정은언니, 민석오빠께 깊

은 감사드립니다. 귀찮은 일 마다하지 않으시고, 항상 곁에서 보살펴주셔서 정말 감사드립니다. 그리고 인자하신 고바야시 선생님, 귀여운 스기모토상, 기꺼이 저의 실험을 도와 며칠 밤을 함께 새준 Ke YANG, 이케나가상, 고바타상, 손박사님, 마찌다상께 감사의 말씀 전합니다. 많은 기회를 주시고 언제나 용기와 격려를 아끼지 않으시고 응원해 주신 것에 진심으로 감사드립니다. 그리고 구조물성I 그룹의 무라야마상, 요시다상, 야쓰다상, 후쿠야마상께 감사의 말씀드립니다. 저의 일본어 실력 향상을 위하여 부단히 애써주시고, 좋은 친구가 되어주셔서 정말 감사합니다. 그리고 키노시타상을 비롯한 분광물성II 그룹의 연구원들과 보이지 않는 곳에서 저를 도와주신 미요시상과 토쿠나가상께도 깊은 감사드립니다. 그밖에 6개월간 여러모로 저를 보살펴주신 많은 분들께 다시 한번 감사드립니다.

마지막으로 언제나 저를 믿어주시고 응원해주시는 저희 부모님께 깊은 감사드립니다. 표현에 서툴고 무뚝뚝한 저를 언제나 사랑으로 감싸주시는 부모님이 계셨기에 지금의 제가 있을 수 있었습니다. 믿어주시는 만큼 스스로의 행동에 책임을 질 수 있는 사람이 되도록 노력하겠습니다. 그리고 나의 가장 가까운 친구이자 훌륭한 조언자인 우리언니와 지금은 군생활을 하고 있는 동생 진수에게도 고마운 마음을 전합니다. 함께 있어 언제나 즐겁고 행복한 우리가족이 있어 정말 큰 힘이 됩니다.

지금은 한없이 부족하고 모자라지만, 배우는 사람의 마음가짐을 잃지 않고 열심히 배워나가도록 하겠습니다. 나태해지지 않고 게으름 피우지 않으며 성실하게 스스로를 채워나갈 수 있도록 노력하겠습니다.